

1 On the formation of hydrothermal vents and cold seeps in the 2 Guaymas Basin, Gulf of California

3 Sonja Geilert¹, Christian Hensen¹, Mark Schmidt¹, Volker Liebetrau¹, Florian Scholz¹,
4 Mechthild Doll², Longhui Deng³, Annika Fiskal³, Mark A. Lever³, Chih-Chieh Su⁴, Stefan
5 Schlömer⁵, Sudipta Sarkar⁶, Volker Thiel⁷, Christian Berndt¹

6
7 ¹GEOMAR Helmholtz Centre for Ocean Research Kiel, Wischhofstraße 1-3, 24148 Kiel, Germany

8 ²Universität Bremen, Klagenfurter-Straße 4, 28359 Bremen, Germany

9 ³Department of Environmental Systems Science, ETH Zurich, Universitätstrasse 16, 8092 Zurich,
10 Switzerland

11 ⁴Institute of Oceanography, National Taiwan University, No. 1, Sec. 4, Roosevelt Road, Taipei 106,
12 Taiwan

13 ⁵Federal Institute for Geosciences and Natural Resources, Stilleweg 2, 30655 Hannover, Germany

14 ⁶Department of Earth and Climate Science, Indian Institute of Science Education and Research Pune,
15 Dr. Homi Bhabha Road, Maharashtra-411008, India

16 ⁷Geobiology, Geoscience Centre, Georg-August University Göttingen, Goldschmidtstr. 3, 37077
17 Göttingen, Germany

18 **Abstract**

19
20
21 Magmatic sill intrusions into organic-rich sediments cause the release of thermogenic CH₄
22 and CO₂. Pore fluids from the Guaymas Basin (Gulf of California) - a sedimentary basin with
23 recent magmatic activity – were investigated to constrain the link between sill intrusions and
24 fluid seepage as well as the timing of sill-induced hydrothermal activity. Sampling sites were
25 close to a hydrothermal vent field at the northern rift axis and at cold seeps located up to 30
26 km away from the rift. Pore fluids close to the active hydrothermal vent field showed a slight
27 imprint by hydrothermal fluids and indicated a shallow circulation system transporting
28 seawater to the hydrothermal catchment area. Geochemical data of pore fluids at cold seeps
29 showed a mainly ambient diagenetic fluid composition without any imprint related to high
30 temperature processes at greater depth. Seep communities at the seafloor were mainly
31 sustained by microbial methane, which rose along pathways formed earlier by hydrothermal
32 activity, driving anaerobic oxidation of methane (AOM) and the formation of authigenic
33 carbonates.

34 Overall, our data from cold seep sites suggest that sill-induced hydrothermalism is not active
35 away from the ridge axis at present and vigorous venting of hydrothermal fluids is restricted
36 to the ridge axis. Using the sediment thickness above extinct conduits and carbonate dating,

37 we calculated that deep fluid and thermogenic gas flow ceased 28 to 7 kyrs ago. These
38 findings imply a short lifetime of hydrothermal systems limiting the time of unhindered
39 carbon release as suggested in previous modeling studies. Consequently, activation and
40 deactivation mechanisms of these systems need to be better constrained for the use in
41 climate modeling approaches.

42

43 **1 Introduction**

44

45 Abrupt climate change events in Earth's history have been partly related to the injection of
46 large amounts of greenhouse gases into the atmosphere (e.g. Svensen et al., 2004; Gutjahr
47 et al., 2017). Among the most prominent of these events was the Paleocene-Eocene Thermal
48 Maximum (PETM) during which the Earth's atmosphere warmed by about 8°C in less than
49 10,000 years (Zachos et al., 2003). The PETM was possibly triggered by the emission of about
50 2000 Gt of carbon (Dickens, 2003; Zachos et al., 2003). Processes discussed to release these
51 large amounts of carbon in a relatively short time are gas hydrate dissociation, volcanic
52 eruptions as well as igneous intrusions into organic-rich sediments, triggering the release of
53 carbon during contact metamorphism (Svensen et al., 2004; Aarnes et al., 2010; Gutjahr et
54 al., 2017).

55 The Guaymas Basin in the Gulf of California is considered as one of the few key sites to study
56 carbon release in a rift basin exposed to high sedimentation rates. A newly discovered vent
57 field in the Guaymas Basin, which releases large amounts of CH₄ and CO₂ up to several
58 hundred of meters into the water column (Berndt et al., 2016), stimulated the discussion on
59 the climate potential of magmatic intrusions into organic-rich sediments (e.g. Svensen et al.
60 2004).

61 The Gulf of California is located between the Mexican mainland and the Baja California
62 Peninsula, north of the East Pacific Rise (EPR; Fig. 1). The spreading regime at EPR continues
63 into the Gulf of California and changes from a mature, open ocean-type to an early-opening
64 continental rifting environment with spreading rates of about 6 cm yr⁻¹ (Curry & Moore,
65 1982). Its spreading axis consists of two graben systems (northern and southern troughs)
66 offset by a transform fault (Fig. 1). The Guaymas Basin, which is about 240 km long, 60 km
67 wide, and reaching water depths of up to 2000 m, is known as a region of vigorous
68 hydrothermal activity (e.g. Curry and Moore, 1982; Gieskes et al., 1982; Von Damm et al.,

69 1985). Hydrothermal activity in the Guaymas Basin was first reported in the southern trough
70 (e.g. Lupton, 1979; Gieskes et al., 1982; Campbell and Gieskes, 1984; Von Damm et al.,
71 1985). Here, fluids emanate partly from Black Smoker type vents at temperatures of up to
72 315°C (Von Damm et al., 1985). The rifting environment in the Guaymas Basin shows a high
73 sediment accumulation rate of up to 0.8-2.5 m kyr⁻¹ resulting in organic-rich sedimentary
74 deposits of several hundreds of meters in thickness (e.g. Calvert, 1966; DeMaster, 1981;
75 Berndt et al., 2016). The high sedimentation rate is caused by high biological productivity in
76 the water column and influx of terrigenous matter from the Mexican mainland (Calvert,
77 1966). Sills and dikes intruding into the sediment cover have a substantial impact on the
78 distribution of heat flow, other environmental conditions and thus early-diagenetic
79 processes within the basin (Biddle et al., 2012; Einsele et al., 1980; Kastner, 1982; Kastner
80 and Siever, 1983; Simoneit et al., 1992; Lizarralde et al., 2010; Teske et al., 2014).

81 Magmatic intrusions and cold seeps at the seafloor were observed up to 50 km away from
82 the rift axis, and a recently active magmatic process triggering the alteration of organic-rich
83 sediments and releasing thermogenic CH₄ and CO₂ was proposed by Lizarralde et al. (2010).
84 These authors attributed elevated CH₄ concentrations and temperature anomalies in the
85 water column to active thermogenic CH₄ production driven by contact metamorphism.
86 According to Lizarralde et al. (2010) ongoing off-axis hydrothermal activity may cause a
87 maximum carbon flux of 240 kt C yr⁻¹ through the seafloor into the ocean and potentially
88 into the atmosphere. However, modelling studies investigating the lifetime of such sill-
89 induced hydrothermalism show that initial CH₄ and CO₂ release is intense and vigorous, but
90 can decline just as quickly (<10 kyr) (Bani-Hassan, 2012; Iyer et al., 2017).

91 During the expedition SO241 by RV SONNE in June/ July 2015 a new hydrothermal vent field
92 was discovered at the flank of the northern trough (Fig. 1; Berndt et al., 2016). The
93 discovered mound rises up to 100 m above the seafloor and predominantly Black Smoker-
94 type vents suggest similar endmember temperatures and geochemical composition as found
95 at the southern trough (Von Damm et al., 1985; Von Damm, 1990; Berndt et al., 2016). The
96 hydrothermal vent system emits methane-rich fluids with a helium isotope signature
97 indicative of fluids in contact with mid-ocean ridge basalt (Berndt et al., 2016). On this
98 cruise, we sampled this recently discovered hydrothermal vent field and some of the off-axis
99 seeps above sill intrusions described by Lizarralde et al. (2010). The aim of this study was to
100 investigate fluid and gas compositions of the off-axis seeps in order to identify the influence

101 of sill intrusions on fluid circulation, gas composition, and the timing of hydrothermal
102 activity. The overall motivation was thus to explore the regional and temporal extent of
103 hydrothermal activity in the area and to provide better constraints on carbon release from
104 sedimented ridge systems.

105

106 **2 Materials and methods**

107 2.1 Sampling devices and strategy

108

109 During the RV SONNE expedition SO241 seven sites across the central graben of the
110 Guaymas basin were investigated (Fig. 1). Site-specific sampling and data recording were
111 performed using (1) a video-guided multicorer (MUC), (2) a gravity corer (GC), (3)
112 temperature loggers attached to a GC or sediment probe, (5) a video-guided VCTD / Rosette
113 water sampler, and (6) a video-guided hydraulic grab (VgHG). Sites were selected according
114 to published data on the locations of seeps (Lizarralde et al., 2010) and seismic data acquired
115 during the cruise (see below).

116

117 2.1.1 Seismic data recording

118

119 Seismic data were collected using a Geometrics GeoEel Streamer of 150 and 183.5 m length
120 and 96 and 112 channels, respectively. Two generator-injector guns in harmonic mode
121 (105/105 cubic inch) served as the seismic source. Processing included navigation processing
122 (1.5625 m crooked line binning), 20, 45, 250, 400 Hz frequency filtering, and poststack Stolt
123 migration with water velocity yielding approximately 2 m horizontal and 5 m vertical
124 resolution close to the seafloor.

125

126 2.1.2 Sediment and pore fluid sampling

127

128 At seepage and vent sites, the video-guided MUC was used to discover recent fluid release,
129 which was indicated by typical chemosynthetic biological communities at the seafloor
130 (microbial mats, bivalves, etc.; Sahling et al., 2002). However, small-scale, patchy
131 distributions of active seepage spots and visibility of authigenic carbonate concretions made
132 it difficult to select the best locations for coring. Hence, the comparison of results from

133 different seeps might be biased in this regard as not all seepage areas could be sampled at
134 their most active places. GC deployments were typically performed at sites initially investigated
135 with the MUC video system or at the center of suspected seeps (based on bathymetry and seismic
136 data).

137 In total, we present pore fluid and gas data collected at the seepage sites North (GC01,
138 MUC11), Central (GC03, GC13, GC15, MUC04), and Ring Seep (MUC05), one reference site
139 (see below; Reference Site; GC04, MUC02), and the hydrothermal vent field (Smoker Site;
140 GC09, GC10, MUC15, MUC16). The Reference Site, that did not show active seepage or faults
141 indicated by seismic data, was chosen to obtain geochemical background values. In addition,
142 the slope towards the Mexican mainland was sampled as well (Slope Site; GC07) (Fig. 1,
143 Table 1). Immediately after core retrieval, GCs were cut, split, and subsampled. Samples
144 were transferred into a cold lab at 4°C and processed within 1 or 2 hours. Pore fluids were
145 obtained by pressure filtration (e.g. Jahnke et al., 1982). After MUC retrieval, bottom water
146 was sampled and immediately filtered for further analyses. The sediment was transferred
147 into a cold lab and sampling was executed in an argon-flushed glove bag. Pore fluids were
148 retrieved by centrifugation and subsequent filtration using 0.2 µm cellulose acetate
149 membrane filters (e.g. Jahnke et al., 1982). Sediment samples (2 cm³) for hydrocarbon
150 analyses were taken using cut-off 3-mL syringes. All hydrocarbon samples were taken
151 immediately after sediment surfaces were exposed after core cutting or sectioning, ensuring
152 minimal disturbance to sediment surfaces prior to sampling and transferred to vials
153 containing concentrated NaCl solution (after Sommer et al., 2009). MUCs were extruded and
154 sampled from the top. GCs were sampled at the bottom ends of 1-m core sections, either at
155 the core catcher or at freshly cut section ends. In some cases additional samples were taken
156 from within GC core sections by cutting the core liner with an oscillating saw, and inserting
157 cut-off syringes into the sides of core sections.

158

159 2.1.3 Subseafloor temperature measurements

160

161 Temperature gradients and thermal conductivity were measured at North Seep, Central
162 Seep, Reference Site, and Smoker Site as well as along a transect across the newly
163 discovered hydrothermal vent field and the rift valley (Graben Site). Miniaturized
164 temperature loggers (MTL) were attached to GCs or to a 5 m long sediment lance at a

165 sampling rate of 1 measurement per second. The absolute accuracy of these temperature
166 measurements was about 0.1 K and the temperature resolution was 0.001 K (Pfender and
167 Villinger, 2002).

168 Thermal conductivity was measured on recovered core material in close vicinity to the MTLs
169 using the KD2 Pro Needle Probe instrument. For temperature measurements obtained by a
170 lance, a constant thermal conductivity of $0.7 \text{ W m}^{-1} \text{ K}$ was assumed. Data processing was
171 done according to Hartmann and Villinger (2002).

172

173 2.1.4 Water column sampling

174

175 Water samples were taken by using a Niskin Water sampler Rosette System equipped with a
176 video camera designed for near-seafloor sampling (Schmidt et al., 2015) in order to study
177 water column chemistry (i.e. dissolved CH_4) and oceanographic parameters (i.e.
178 temperature, salinity, turbidity). Eight water sampling locations were chosen in the vicinity
179 of MUC and GC stations and were termed North Seep (VCTD03), Central Seep (VCTD02), Ring
180 Seep (VCTD01), Graben Site (CTD01; no video-guided sampling), Smoker Site (VCTD06 and
181 10), and Slope Site (VCTD07). The (V)CTDs were either used in a towed mode (VCTD03, 06,
182 09, 10) or in station (CTD01; VCTD01, 02, 07) keeping hydrocast mode. The water depth was
183 controlled based on pressure readings, altitude sensors (<50 m distance to bottom), and
184 online video observation (1 - 2 m above the seafloor).

185

186 2.1.5 Authigenic carbonate sampling

187

188 At Central Seep a block (approx. $1 \times 0.5 \times 0.3 \text{ m}$) was recovered using a video-guided
189 hydraulic grab (VgHG, GEOMAR) in 1843 m water depth from the surface of a typical cold
190 seep environment (close to high abundance of tube worms) . The block consisted mainly of
191 solidified carbonate matrix covered by a whitish carbonate rim and was characterized by
192 coarse open pore space in mm to cm scale (see supplementary Fig. S1).

193

194 2.2 Sample treatment and analytical procedures

195

196 Pore fluids were analyzed onboard for total dissolved sulfide (TH₂S) and NH₄ directly after
197 recovery by photometry using standard methods described in Grasshoff et al. (2002). Prior
198 to NH₄ measurements, pore fluids containing dissolved sulfide were treated with argon to
199 prevent biased NH₄ measurements. Total alkalinity (TA) was determined by titration
200 immediately after pore water separation using 0.02 M HCl (Ivanenkov and Lyakhin, 1978).
201 Shore-based analyses of the remaining acidified pore water included dissolved anions (SO₄,
202 Cl) and cations (Li, Mg) using ion chromatography (IC, METROHM 761 Compact, conductivity
203 mode) and inductively coupled plasma optical emission spectrometry (ICP-OES, VARIAN 720-
204 ES), respectively. All chemical analyses were tested for accuracy and reproducibility using the
205 IAPSO salinity standard (Gieskes et al., 1991).

206
207 Strontium isotope ratios were analyzed by Thermal Ionization Mass Spectrometry (TIMS,
208 Triton, ThermoFisher Scientific). The samples were chemically separated via cation exchange
209 chromatography using the SrSpec resin (Eichrom). The isotope ratios were normalized to the
210 NIST SRM 987 value of 0.710248 (Howarth and McArthur, 2004) which reached a precision
211 of ± 0.000015 (2 sd, n = 12). Potential influences of ⁸⁷Rb interferences on ⁸⁷Sr/⁸⁶Sr isotope
212 ratios were eliminated by combining the highly selective Sr-Spec resin and Rb/Sr-
213 discriminating TIMS pre-heating procedures with the static mode measurement of ⁸⁵Rb
214 simultaneously to the Sr masses 84, 86, 87 and 88 for optional Rb/Sr corrections (not
215 required in this study).

216 Water samples taken from Niskin bottles were transferred into 100 ml glass vials with helium
217 headspace of 5 ml and poisoned with 50 µl of saturated mercury chloride solution.

218 Hydrocarbon composition of headspace gases was determined using a CE 8000 TOP gas
219 chromatograph equipped with a 30 m capillary column (Restek Q-PLOT, 0.32 mm) and a
220 flame ionization detector (FID). Replicate measurements yielded a precision of <3 % (2 sd).

221 Stable carbon isotopes of methane were measured using a continuous flow isotope ratio
222 mass spectrometer (cf-IRMS). A Thermo TRACE gas chromatograph was used to separate the
223 light hydrocarbon gases by injecting up to 1 ml headspace gas on a ShinCarbon ST100/120
224 packed gas chromatography column. The separated gases were combusted and
225 corresponding δ¹³C values were determined using a Thermo MAT 253 mass spectrometer.
226 The reproducibility of δ¹³C measurements was ±0.3 ‰ (2 sd) based on repeated
227 measurements of the reference standard Vienna Pee Dee Belemnite (VPDB).

228 Stable hydrogen isotope compositions of methane were analyzed by separating methane
229 from other gases by online gas chromatography (Thermo Trace GC; isotherm at 30°C; 30 m
230 RT-Q-Bond column, 0.25 mm ID, film thickness 8 μm). Methane-H was reduced to
231 dihydrogen at 1420°C prior to stable isotope analysis using a coupled MAT 253 mass
232 spectrometer (Thermo). Data are reported in per mil relative to Standard Mean Ocean
233 Water (SMOW). The precision of δD-CH₄ measurements was ±3 ‰ (2 sd).

234
235 ²¹⁰Pb (46.52 keV) and ²¹⁴Pb (351.99 keV) were simultaneously measured on freeze dried
236 sediments by two HPGe gamma spectrometry systems (ORTEC GMX-120265 and GWL-
237 100230), each interfaced to a digital gamma-ray spectrometer (DSPECPlus™). Efficiency
238 calibration of the gamma detectors were calibrated using IAEA reference materials (for
239 GMX-type detector: 327A, 444 spiked soil, CU-2006-03 spiked soil, RGTh and RGU for sample
240 weight at 100 g; for well-type detector: IAEA-RGTh and RGU from 0.5 to 3.5 g), coupled with
241 an in-house secondary standard ('Rock-falling Mountain soils', Radiation Monitoring Center
242 of the Atomic Energy Council, Taiwan) for various masses (Lee et al., 2004; Huh et al., 2006).
243 ²¹⁴Pb was used as an index of ²²⁶Ra (supported ²¹⁰Pb) whose activity concentration was
244 subtracted from the total ²¹⁰Pb to obtain excess ²¹⁰Pb (²¹⁰Pb_{ex}). The activities of radionuclides
245 were decay-corrected to the date of sample collection. All radionuclide data were calculated
246 on salt-free dry weight basis.

247
248 A representative sample of the authigenic carbonate (cm-scale) was broken from the upper
249 surface of the block, gently cleaned from loosely bound sediment and organic remains and
250 dried at 20°C for 12 h. Two different subsamples were prepared by drilling material with a
251 handheld mm-sized mini-drill from the outer rim (whitish coating, lab code: 470-15) and the
252 related inner core (dark matrix, lab code: 472-15).

253 Prior to aliquot procedures both subsamples were finely ground in an agate mortar
254 providing homogeneous aliquots of suitable grain size for mineral identification by X-ray
255 diffractometry (XRD) (Philips X-ray diffractometer PW 1710 in monochromatic CuKα mode
256 between 2 and 70 2θ (incident angle), for details see supplement). Subsamples were
257 analyzed for δ¹⁸O and δ¹³C by stable isotope ratio mass spectrometry (SIRMS) and U-Th
258 geochronology by multi collector-inductively coupled plasma-mass spectrometry (MC-ICP-
259 MS) on a parallel leachate / sequential dissolution approach for single and isochron ages

260 (method see supplement). Furthermore, $^{87}\text{Sr}/^{86}\text{Sr}$ isotope signatures for aliquots of the
261 individual U-Th solutions by thermal ionization mass spectrometry (TIMS, for method details
262 please refer to pore water Sr isotope analyses) were determined. Lipids extracts for
263 biomarker analyses were determined as well (see below).

264
265 From each homogenized carbonate powder sample (see above), an aliquot of 10 mg was
266 separated for carbon $\delta^{13}\text{C}$ and oxygen $\delta^{18}\text{O}$ stable isotope analysis. A fraction from this
267 (approximately 1 mg) was dissolved by water-free phosphoric acid at 73°C in a “Carbo-Kiel”
268 (Thermo Fischer Scientific Inc.) online carbonate preparation line and measured for carbon
269 and oxygen stable isotope ratios with a MAT 253 mass spectrometer (Thermo-Fischer Inc.).
270 The $\delta^{13}\text{C}$ and $\delta^{18}\text{O}$ values were calculated as deviations from laboratory standard referred to
271 the PDB scale and reported in ‰ relative to V-PDB. The external reproducibility was checked
272 by replicate analyses of laboratory standards as being better than ± 0.04 ‰ for $\delta^{13}\text{C}$ and ± 0.1
273 ‰ for $\delta^{18}\text{O}$ (1 sd, $n=7$) for this sample set. However, the single measurement uncertainties
274 were significantly better and the resulting 2 sd ($n=3$) for both main samples are given in the
275 supplement Table S5.

276
277 Biomarkers were extracted from 4 g of powdered sample and were then sequentially
278 extracted with dichloromethane (DCM)/methanol (3/1, v/v), DCM, and *n*-hexane
279 (ultrasonication, 20 min). The combined extracts were dried, derivatized using a
280 BSTFA/trimethylchlorosilane mixture (95/5, v/v; 1h; 40°C) and analyzed by coupled gas
281 chromatography-mass spectrometry (GC-MS; Hinrichs et al., 2000). GC-MS analyses were
282 carried out with a Thermo Fisher Trace 1310 GC coupled to a Quantum XLS Ultra MS. The
283 instrument was equipped with a Phenomenex Zebron ZB 5MS capillary column (30 m, 0.1
284 μm film thickness, inner diameter 0.25 mm). Fractions were injected splitless at 270°C. The
285 carrier gas was He (1.5 mL/min). The GC oven temperature was ramped from 80°C (1 min) to
286 310°C at 5°C min^{-1} and held for 20 min. Electron ionization mass spectra were recorded at 70
287 eV.

288

289 **3 Results**

290 3.1 Subsurface structure and evidence for sill-related fluid mobilization

291

292 Seismic profiles showed a wide range of sediment deformation (Fig. 2). Seismic amplitude
293 blanking along vertical zones below the seafloor indicated the flow of gaseous pore fluids at
294 North, Central, and Ring Seep (Fig. 2). Underneath these locations sediments were
295 deformed, probably due to sediment mobilization associated with hydrothermal activity in
296 response to sill intrusion. In contrast the Reference Site sediments showed a more or less
297 continuous succession without vertical disturbance. At North Seep, a shallow high-amplitude
298 reversed polarity reflector occurred at 50-60 ms. Sill depths were inferred from the seismic
299 profiles at ~500 to 600 meter below seafloor (mbsf) for North Seep and with ~350 to 400
300 mbsf at the other sites, assuming seismic interval velocities of 1600 to 2000 m s⁻¹. Seismic
301 images suggest that massive disturbance of sediments and vertical pipe structures are
302 related to channeled fluid and/or gas advection caused by sill intrusions (Fig. 2). Faults are
303 indicated which may serve as fluid pathways above potential sill intrusions. Closer inspection
304 of the seismic reflectors at the Central Seep (Fig. 2c) shows onlap onto a doming structure.
305 On the NW flank of the dome the deepest onlap occurs at 60 ms or 48 mbsf (assuming 1600
306 m s⁻¹ sediment interval velocity) whereas on the SE flank the shallowest onlap occurs at 15
307 ms or 12 mbsf.

308

309 3.2 Temperature measurements

310

311 Heat flow and temperature gradients were measured at North and Central Seep, Reference
312 Site, and Smoker Site (attached to GCs) as well as in transects along the hydrothermal ridge
313 and rift axis (attached to a temperature lance; Fig. 3 and S2, Table 1). Temperature gradients
314 are shown in Figure S2. Highest heat flows occurred close to the Smoker Site and ranged
315 between 599 and 10835 mW m⁻². Temperature gradients were also highest at the Smoker
316 Site (~15 K m⁻¹). In contrast, heat flows and temperature gradients in the rift valley close to
317 the rift axis ranged between 262 and 338 mW m⁻² and 0.4 to 0.5 K m⁻¹, respectively.
318 Generally heat flow values decreased with increasing distance to the rift axis with 140 mW
319 m⁻² at the Reference Site, 113 mW m⁻² at Central Seep, and 28 mW m⁻² at North Seep.
320 Temperature gradients were 0.22 K m⁻¹ at the Reference Site, 0.16 K m⁻¹ at Central Site and
321 0.14 K m⁻¹ at North Site.

322

323 3.3 Sediment characteristics and sedimentation rates

324

325 The sediments were mainly composed of organic-rich diatomaceous clay, consistent with
326 earlier analyses (e.g. Kastner, 1982). At North Seep, the sediments were composed of
327 homogeneous diatomaceous clay containing rare shell fragments and carbonate
328 concretions. Gas hydrates were discovered at 2.5 mbsf. Authigenic carbonates were exposed
329 at the seafloor. At Ring Seep, SW of North Seep, sediments were predominantly composed
330 of diatomaceous clay. At Central Seep, located between North Seep and Smoker Site,
331 sediments were composed of homogeneous diatomaceous clay intercalated with whitish
332 layers and shell fragments occurring shallow in the sediment ($\leq 70\text{cm}$). Again, authigenic
333 carbonates were observed on the seafloor. At Smoker Site, ca. 500 m SE of the hydrothermal
334 vent field, surface sediments were likewise composed of diatomaceous clay with light and
335 dark greyish banding. Traces of bioturbation were visible in the upper 4 m. At this depth, a
336 sharp contact defined the transition to the underlying hydrothermal deposits, which were
337 composed of mm-to-cm sized black to grey Fe-rich sulfides (for a detailed description see
338 Berndt et al. (2016)). Within the hydrothermal deposits brownish to grey clay lenses
339 appeared. At the Slope Site, sediments were laminated in the mm- to cm-range. The
340 sediment was dominated by diatomaceous clay that contained a few ash lenses.
341 The sedimentation rates ranged between 0.4 m kyr^{-1} at Smoker Site and 3.5 m kyr^{-1} at North
342 Seep based on radionuclide measurements (Table 1). Sedimentation rates at all other sites
343 were about 2 m kyr^{-1} .

344

345 3.4 Pore water geochemistry

346

347 All pore water data and isotope measurements of $^{87}\text{Sr}/^{86}\text{Sr}$ are listed in supplementary
348 Tables S1 and S2. Pore water profiles of TA, TH_2S , SO_4 , CH_4 , NH_4 , Cl, Mg, and Li are shown in
349 Fig. 4a (GCs) and 4b (MUCs).

350

351 Pore water constituents plotted in Figure 4 were selected to characterize variations in
352 organic matter diagenesis, anaerobic oxidation of methane (AOM), as well as potential
353 water-rock interactions related to subsurface hydrothermal activity. In general, methane
354 concentrations were elevated at the seep locations and at the slope, thus enhancing AOM.
355 TA and TH_2S increased with depth for North Seep, Central Seep (only MUC04), and Slope

356 Site, while SO_4 was decreasing. AOM depths could only be inferred for North Seep with ~160
357 cm and Slope Site with ~300 cm. NH_4 was only slightly increasing with depth; higher NH_4 -
358 levels were only found at the Slope Site (Fig. 4). Concentrations of Cl, Mg, and Li did not
359 show significant variations from seawater in shallow sediment depths (MUCs). At greater
360 depths (GCs) some deviations from seawater concentration occurred at North Seep, Smoker
361 Site, and Slope Site. At North Seep, Mg showed a minor offset at ~150 cm depth, while at
362 Smoker Site Mg concentrations increased continuously. In GC09 at Smoker Site, Li
363 concentrations increased and Mg concentrations decreased abruptly in a depth of ~400 cm.
364 At the Slope Site, Mg increased slightly below 400 cm sediment depth while Li showed a
365 small decrease above 400 cm.

366 Sr concentrations and isotopes are plotted in Fig. 5. Sr concentrations showed
367 predominantly modern seawater values, except at North Seep where they strongly
368 decreased. The $^{87}\text{Sr}/^{86}\text{Sr}$ isotope ratios also showed predominantly seawater values
369 (0.709176; Howarth and McArthur, 2004), except for the Smoker Site where the isotope
370 ratios decreased strongly below the transition between hemipelagic sediments and
371 hydrothermal deposits (Fig. 5). North and Ring Seeps as well as Smoker Site (GC10) showed
372 slight decreases in $^{87}\text{Sr}/^{86}\text{Sr}$. The ratios showed a similar depletion as those from the
373 hydrothermal plume (Berndt et al., 2016).

374

375 3.5 Hydrocarbon gases, carbon and hydrogen isotope data

376

377 Concentrations of dissolved hydrocarbons and $\delta^{13}\text{C}_{\text{CH}_4}$, $\delta^{13}\text{C}_{\text{C}_2\text{H}_6}$, and $\delta\text{D}_{\text{CH}_4}$ data are reported
378 in supplementary Table S3. Overall, our pore fluid data showed a large variability in
379 $\text{CH}_4/(\text{C}_2\text{H}_6+\text{C}_3\text{H}_8)$ with ratios between 100 and 10,000 and $\delta^{13}\text{C}_{\text{CH}_4}$ between -26.5 and -88.2
380 ‰. Gas hydrate $\delta^{13}\text{C}_{\text{CH}_4}$ ranged between -57.9 and -58.9 ‰. The $\delta^{13}\text{C}_{\text{C}_2\text{H}_6}$ values ranged
381 between -26.1 and -38.3 ‰ for North Seep and -29.6 and -37.7 ‰ for Central Seep. The
382 $\delta\text{D}_{\text{CH}_4}$ values at both seeps ranged between -97 and -196 ‰, for the gas hydrates between -
383 196 and -198 ‰, for Slope Site between -192 and -196 ‰, and for the hydrothermal plume
384 between -98 and -113 ‰ (VCTD09).

385

386 3.6 Water column data

387

388 Water column characteristics like temperature, salinity, turbidity, and methane
389 concentrations are shown in Fig. 6 and Table S4. Surface waters in the Guaymas Basin
390 showed warm temperatures up to 29.5°C (salinity: 34.5 ‰) close to the Mexican mainland
391 (Slope Site, VCTD07) and up to 24.6°C (salinity: 34.6 ‰) in the central basin (Central Seep,
392 VCTD02). With depth, temperatures decreased continuously and ranged between 2.8 and
393 3.0°C (salinity: 34.6 ‰) close to the seafloor (1600 – 1800 m). Turbidity values were high in
394 the deep water layer (~1400-1800 m) and indicate a well-mixed deep basin, also shown by
395 relatively homogeneous temperature and salinity data. Only the water column directly
396 above the hydrothermal vent field showed strongly elevated temperature (28.4°C) and
397 salinity (35.1 ‰) (Berndt et al., 2016). Methane concentrations were highest close to the
398 hydrothermal vent field (up to 400 μM, (VCTD09 from Berndt et al., 2016), but still varied in
399 the deep water column of the basin between 2 and 28.1 nM (Central Seep (VCTD02) and
400 Ring Seep (VCTD01), respectively).

401

402 3.7 Authigenic carbonate data

403

404 The authigenic carbonate sample (Fig. S1) consisted of 88 to 90 % aragonite and 6 to 12 %
405 calcite (supplementary Table S5). By the uncertainty related maximum deviation of Δd_{104} (<
406 0.01) the XRD spectrum identified calcite with a Mg fraction below 3 % according to
407 Goldsmith et al. (1961). The bulk outer rim carbonate had an average carbon isotope
408 signature ($\delta^{13}\text{C}_{\text{V-PDB}}$) of -46.6 ± 0.2 ‰ and an oxygen isotope signature ($\delta^{18}\text{O}_{\text{V-PDB}}$) of 3.7 ± 0.3
409 ‰. Inner core carbonate isotope signatures yielded similar values with $\delta^{13}\text{C}_{\text{V-PDB}}$ of -44.7 ± 0.4
410 ‰ and $\delta^{18}\text{O}_{\text{V-PDB}}$ of 3.6 ± 0.1 ‰ (Table S5). The average outer rim $^{87}\text{Sr}/^{86}\text{Sr}$ ratio was
411 0.709184 ± 0.000027 and the inner core ratio was 0.709176 ± 0.000003 . The U-Th carbonate
412 dating approach on these authigenic carbonates implied formation ages younger than 240
413 yrs BP.

414 Lipid extracts obtained from seep carbonate 56-VgHG-4 (Central Seep) revealed a strong
415 signal of specific prokaryote-derived biomarkers (Fig. S1). These compounds encompassed
416 isoprenoid lipids derived from archaea namely crocetane, 2,6,10,15,19-
417 pentamethylcosane(-icosenes (PMI, PMIΔ) archaeol, and *sn*2-hydroxyarchaeol (see Fig. S1
418 for structures). In addition, the sample contained a suite of non-isoprenoid 1,2-
419 dialkylglycerolethers (DAGE) of bacterial origin. Typical compounds of planktonic origin, such
420 as sterols, were also present, but low in abundance.

421

422 **4 Discussion**

423 4.1 Origin of seeping fluids

424 4.1.1 Smoker Site

425

426 The water column above the newly discovered hydrothermal vent field exhibits elevated CH₄
427 concentrations (up to 400 μM) and pCO₂ data (>6000 μatm) (Berndt et al., 2016). The range
428 of the measured stable isotope signature of methane ($\delta^{13}\text{C}_{\text{CH}_4}$ between -39‰ and -14.9‰)
429 and the helium isotope anomaly (³He/⁴He ratio of 10.8 x 10⁻⁶) clearly indicate gas exhalations
430 from thermogenic organic matter degradation with contributions from a mantle source (see
431 Berndt et al., 2016). These northern trough hydrothermal fluids are comparable in their gas
432 geochemistry to the southern trough (Lupton, 1979; Von Damm et al., 1985; Berndt et al.,
433 2016). However, the highest heat flow values of up to 10835 mW m⁻² measured in this study
434 are found close to the Smoker Site and are much higher than those observed in earlier
435 studies (maximal 2000 mW m⁻², Fisher and Becker, 1991). The high heat flow at Smoker Site
436 even exceeds the hydrothermally more active southern trough where heat flow values of
437 2000 to 9000 mW m⁻² were measured (Lonsdale and Becker, 1985; Fisher and Becker, 1991).
438 This might indicate that hydrothermal activity at the northern trough is younger and possibly
439 a more recent process compared to the southern trough.

440 Hydrothermal fluids are typically depleted in Mg and highly enriched in fluid-mobile
441 elements like Li caused by high-temperature reactions with mafic rocks (here sills) and/ or
442 sediments through which they percolate (e.g. Einsele et al., 1980; Gieskes et al., 1982;
443 Kastner, 1982; Von Damm et al., 1985; Lizarralde et al., 2010; Teske et al., 2016). Such
444 compositions were reported from DSDP site 477 (Gieskes et al., 1982) and fluids obtained by
445 Alvin dives (Von Damm et al., 1985) (see Fig. 1 for location of Site DSDP 477). Although

446 strongly diluted, CTD samples from the hydrothermal plume in the northern trough show
447 this trend (Berndt et al., 2016).

448 An indication for the presence of hydrothermal fluids in pore waters in the vicinity of the
449 hydrothermal vent field is found at about 4 m depth in core GC09. Here, positive Li and
450 negative Mg concentrations (Fig. 4a) are probably caused by weak admixing of hydrothermal
451 solutions (Gieskes et al., 1982; Hensen et al., 2007). Likewise, $^{87}\text{Sr}/^{86}\text{Sr}$ isotope ratios
452 decrease to a value of 0.708949 (Fig. 5) and thus tend towards the $^{87}\text{Sr}/^{86}\text{Sr}$ ratio of the local
453 hydrothermal endmember ($^{87}\text{Sr}/^{86}\text{Sr} = 0.7052$; Von Damm, 1990). Hydrothermal endmember
454 Li concentrations in the Guaymas Basin have been reported in a range between 630 and
455 1076 μM (Von Damm et al., 1985) and are 20 to 30 times higher than those measured at
456 Smoker Site ($\sim 34 \mu\text{M}$; Fig. 4a, Table S1). Here, hydrothermal fluids account for about 3 % in
457 the mix with seawater (Fig. 7). The sediments in this core section also change from
458 diatomaceous clay to unconsolidated, coarse-grained hydrothermal deposits (Fe-rich
459 sulfides; see also Sect. 3.3) which may facilitate the circulation of hydrothermal fluids.

460 Despite the proximity of the remaining GCs and MUCs to the hydrothermal vent field (~ 500
461 m distance; temperatures immediately after retrieval are up to 60°C) typical pore fluid
462 indicators such as Mg, Li, and $^{87}\text{Sr}/^{86}\text{Sr}$ do not show major excursions from seawater values
463 (Fig. 4). Similarly, NH_4 , an indicator for a diagenetic or catagenetic breakdown of organic
464 matter, is only poorly enriched in sediments surrounding the hydrothermal vents ($\text{NH}_4 \leq 0.3$
465 mM). NH_4 remains well below the value reported from the southern trough (20 mM; Von
466 Damm et al. (1985)) and the Slope Site (GC07) where 10 mM are reached already at
467 subsurface depths of only a few meters (Fig. 4). The pore fluid geochemistry around the
468 hydrothermal vent field therefore confirms that early-diagenetic processes are not intense
469 (Fig. 7) and that the shallow sediments are not significantly affected by hydrothermal fluids.
470 We hypothesize that hydrothermal venting causes a shallow convection cell drawing
471 seawater through the sediments towards the hydrothermal vent field, while the sediments
472 become heated by lateral heat conduction (cf. Gamo et al., 1991; Henry et al., 1996;
473 Kinoshita and Yamano, 1997).

474
475 The diatomaceous clay might act as a seal to upwards migrating fluids, which are channeled
476 to the catchment area of the rising hydrothermal fluids of the hydrothermal vent field (see
477 also Berndt et al., 2016, their Fig. 4). The geochemical composition of these fluids is likely

478 influenced by high temperature chemical alteration of the sediment caused by the intruded
479 sills (Fig. 2b). However, shallower pore fluids of surface sediments at the Smoker Site (i.e. 0-4
480 m) are not much affected by contributions from these fluids and show predominantly
481 ambient diagenetic fluid signatures.

482

483 4.1.2 Cold seeps

484

485 The selection of sampling sites at presumed seep locations was based on existing published
486 data (Lizarralde et al., 2010) and information from seismic records (Fig. 2). Seismic amplitude
487 blanking along vertical zones below the seafloor indicates active fluid and/ or gas conduits at
488 North and Central Seep. Given that sill intrusions and related high-temperature alteration of
489 sediments are driving the seepage, the expectation was to find deeply-sourced (average sill
490 depth ~400 m) fluids with a typical geochemical signature analogous to findings at
491 hydrothermal vents in the Guaymas Basin (Von Damm et al., 1985; Von Damm, 1990; Berndt
492 et al., 2016). Such characteristics are e.g. a high concentration of thermogenic hydrocarbon
493 gases formed by organic-matter degradation, enrichments in NH₄, depletion in Mg, and a
494 strong enrichment in fluid-mobile tracers like Li and B (e.g. Aloisi et al., 2004; Scholz et al.,
495 2009). Hydrocarbon formation caused by abiogenic processes plays only a minor role in the
496 hydrothermal vent field (McDermott et al., 2015; and discussion in Berndt et al. (2016)).

497

498 Samples obtained using a video-guided MUC revealed the highest methane concentrations
499 at North, Central, and Ring Seeps (Fig. 4b). In conjunction with visual evidence (abundant
500 chemosynthetic biological communities) this confirms that we have hit active seepage areas
501 during our sampling campaign. At the two most active sites, North and Central, high
502 methane levels are accompanied by a significant drop in sulfate and increase in TA and TH₂S,
503 providing evidence for AOM, according to the net reaction:

504



506

507 (e.g. Nauhaus et al., 2005; see Wegener et al., 2016 for a recent update).

508 These pore water trends are even more pronounced in GC01 (North) where the AOM zone
509 was completely penetrated and gas hydrate was found at about 2.5 mbsf. Unfortunately,

510 GCs from similarly active sites could not be obtained from Central and Ring Seeps, mainly
511 because of patchiness of seepage spots and widespread authigenic mineralizations at the
512 seafloor preventing sufficient penetration. Nevertheless, active methane seepage at all three
513 investigated sites is evident. The methane flux is, however, not accompanied by any
514 significant excursion of pore water constituents typical for deeply-sourced, high-
515 temperature sediment-water interactions (e.g. Mg, Cl, Li). Also Sr concentrations show
516 seawater values at all seep sites (Fig. 5), except for North Seep where values drop together
517 with Ca due to co-precipitation during carbonate formation. The $^{87}\text{Sr}/^{86}\text{Sr}$ ratios show
518 predominantly seawater signatures as well (Fig. 5, Table S2). Similarly, low NH_4
519 concentrations of <1 mM indicate a low intensity of organic matter decomposition (as
520 discussed in Sect. 4.1.1). Taken together, our data show that, with exception of methane and
521 sulfate, the pore water corresponds to ambient diagenetic conditions that are typically met
522 in this shallow subsurface depth. An explanation for the decoupling of methane levels and
523 pore water composition is that only methane is rising to the seafloor as a free gas. This
524 assumption requires a closer look at the composition of dissolved hydrocarbons in general,
525 which is given below.

526

527 4.2 Origin of hydrocarbon gases

528 4.2.1 Alteration effects

529

530 The origin of hydrocarbon gases can be deciphered by plotting $\text{CH}_4/(\text{C}_2\text{H}_6+\text{C}_3\text{H}_8)$ ratios versus
531 $\delta^{13}\text{C}_{\text{CH}_4}$ data in a modified Bernard diagram (Schmidt et al., 2005 and literature therein) (Fig.
532 8a) and $\delta^{13}\text{C}_{\text{CH}_4}$ versus $\delta\text{D}_{\text{CH}_4}$ after Whiticar (1999) and Welhan (1988) (Fig. 8b). Most of the
533 measured stable isotope data of pore water methane indicate a microbial origin or a mixed
534 microbial and thermogenic origin (Fig. 8). By contrast, hydrocarbons venting at the
535 hydrothermal vent field reflect a mixture of thermogenic methane and abiogenic methane
536 derived from water-rock interactions (Berndt et al., 2016).

537 It has to be considered though that - except of three samples from North Seep - all $\delta^{13}\text{C}_{\text{CH}_4}$
538 measurements were performed on samples located above the AOM zone (see Fig. 4). This
539 implies that the upward-rising methane has likely undergone fractionation due to methane
540 oxidation by sulfate in the AOM zone underneath. AOM enriches DIC in ^{12}C and results in
541 progressively increasing $\delta^{13}\text{C}_{\text{CH}_4}$ values in the residual methane (Whiticar, 1999). Considering

542 the $\delta^{13}\text{C}_{\text{CH}_4}$ at Slope Site as a microbial endmember composition for the Guaymas Basin (Fig.
543 8a), most of the data fall on calculated fractionation lines for AOM following a Rayleigh trend
544 (Whiticar, 1999). Methane sampled close to the Smoker Site (MUC15) is obviously also
545 affected by AOM (Fig. 8a). This is in line with recent studies on hydrothermal sediments of
546 the southern trough of the Guaymas Basin, where bacterial and archaeal communities
547 catalyze the oxidation of methane and higher hydrocarbons and shift $\delta^{13}\text{C}_{\text{CH}_4}$ values to
548 heavier signatures (Dowell et al., 2016).

549 The origin of methane and oxidation effects can further be identified in the $\delta^{13}\text{C}_{\text{CH}_4}$ versus
550 $\delta\text{D}_{\text{CH}_4}$ plot after Whiticar (1999) and Welhan (1988) (Fig. 8b). Slope Site samples plot in the
551 field of microbial CO_2 reduction while hydrothermal plume samples plot in the thermogenic
552 field. One sample even points to a mantle signature, and thus shows potential endmember
553 isotope signatures (Berndt et al., 2016). North Seep samples (pore fluids and gas hydrates)
554 plot in the mixing region while samples from Central Seep clearly shift away from the
555 microbial field and are considered to be affected by bacterial oxidation (Whiticar, 1999).

556 Considering the methane below the AOM as being unaltered, three North Seep samples and
557 the majority of the Slope Site samples show a clear microbial source of methane (Fig. 8a). All
558 other samples appear to be affected by major oxidation following a Rayleigh fractionation
559 process and show that only a fraction between 2 % (MUC04, Central Seep) and 0.05 %
560 (GC15, Central Seep) remains as unoxidized methane (Fig. 8a).

561

562 4.2.2 Origin of unaltered samples

563

564 The $\delta^{13}\text{C}_{\text{CH}_4}$ versus $\delta\text{D}_{\text{CH}_4}$ plot of unaltered North Seep samples suggests a mixing of microbial
565 and thermogenic methane (Fig. 8b). Similar signals have also been observed at Hydrate
566 Ridge (Milkov et al., 2005) and seem to be a common phenomenon in hydrothermal and
567 cold seep affected sediments. In a few samples from North and Central Seep ethane
568 concentrations have been high enough to measure stable carbon isotopes and the $\delta^{13}\text{C}_{\text{C}_2\text{H}_6}$
569 values point to a thermogenic origin (Table S3).

570

571 4.3 Timing of active (thermogenic) methane release

572 4.3.1 Seep site geochemistry

573

574 Based on our data set no deep-sourced fluid is currently migrating upwards at the cold seeps
575 investigated (compare deep-sourced seepage sites from the Gulf of Cadiz in Fig. 7). Hence, in
576 terms of the original hypothesis that fluid emanation is directly linked to recent sill
577 intrusions, these cold seep sites cannot be considered as being active as claimed by
578 Lizarralde et al. (2010). These authors argued that thermogenic carbon is currently released
579 up to 50 km away from the rift axis causing a maximum carbon flux of 240 kt C yr^{-1} . Further,
580 Lizarralde et al. (2010) showed temperature anomalies, high methane concentrations, and
581 helium isotopic anomalies in the water column potentially indicative of a magmatic source.
582 These anomalies were detected in close vicinity to bacterial mats, tubeworms, and
583 authigenic carbonates, situated above areas of sill intrusions. Comparable structures have
584 been identified in this study by video-guided MUCs and seismic data (Fig. 2). Our detailed
585 results on pore fluid, water column, and gas geochemistry now show that most methane
586 was of microbial origin (Fig. 8) and only traces of thermogenic methane were found up to
587 ~ 20 km off axis (North Seep). Even pore fluids taken close to the hydrothermal vent field are
588 dominated by shallow microbial degradation processes, indicating that hydrothermal fluid
589 flow in the Guaymas Basin is rather localized and bound to focused fluid pathways. The
590 temperature and chemical anomalies detected by Lizarralde et al. (2010) might also arise
591 from the deep water layer in the Guaymas Basin itself which is influenced by hydrothermal
592 fluids (Campbell and Gieskes, 1984). Hydrothermal activity in the Guaymas Basin produces
593 hydrothermal plumes which are rising 100-300 m above seafloor and spreading out along
594 density gradients throughout the basin (Campbell and Gieskes, 1984). Our results
595 nevertheless show that the Guaymas Basin has a well-mixed bottom seawater layer with
596 temperatures ranging between 2.8 and 3.9°C in >1000 m depth and off-axis methane
597 concentrations that vary quite considerably (e.g. 6 to 28 nM at Ring Seep, Fig. 9). These
598 bottom seawater variabilities are bigger than the reported anomalies by Lizarralde et al.
599 (2010) and might indicate that thermogenic methane release might not be as widespread as
600 suspected before.

601 Pore fluids taken in a transect up to ~ 30 km away from the rift axis show no evidence for
602 high-T reactions (Fig. 4, 7). We can still not exclude the possibility that thermogenic methane
603 is released in other areas of the basin, but the lack of evidence for high temperature
604 geochemical processes at our sites is evident and clearly contradicts with the conclusions

605 drawn by Lizarralde et al. (2010). Our findings suggest that a projection of the thermogenic
606 methane release based on the number of detected sills (Lizarralde et al., 2010) represents a
607 maximum estimate as it does neither consider the time of the emplacement of a sill nor the
608 lifetime of such magmatic systems. Today, shallow microbial degradation processes
609 determine pore fluid signatures (Fig. 4, 8). Whereas high temperature thermogenic reactions
610 have certainly been active during sill emplacement and once released large amounts of
611 carbon, these processes have apparently ceased. However, pipe structures may still act as
612 high-permeability pathways and facilitate the advection of gas. As a result, small amounts of
613 thermogenic carbon might be released as reflected by the signatures of $\delta^{13}\text{C}_{\text{CH}_4}$ and
614 thermogenic $\delta^{13}\text{C}_{\text{C}_2\text{H}_6}$ isotope data at North and Central Seep. However, present methane
615 advection rates are slow (probably $<1 \text{ cm yr}^{-1}$) as observed by low methane gradients in the
616 pore fluid profiles (Fig. 4). These conditions favor an effective turnover of CH_4 to bicarbonate
617 and authigenic carbonates by AOM (Wallmann et al., 2006; Karaca et al., 2010).

618

619 4.3.2 Origin of the authigenic carbonate

620

621 The porous authigenic carbonate block recovered from the seafloor at Central Seep can
622 preserve long-term information about seepage in this area. The predominant biomarkers
623 found in the seep carbonate from the Central Site (56-VgHG-4) are consistent with microbial
624 consortia performing AOM. In particular, high abundances of crocetane and *sn*2-
625 hydroxyarchaeol indicate major contributions from methanotrophic archaea of the ANME-2
626 cluster, whereas DAGE originate from syntrophic sulfate-reducing bacteria, probably of the
627 *Desulfosarcina–Desulfococcus* group (Blumenberg et al., 2004; Niemann and Elvert, 2008).
628 These consortia gain energy from AOM with sulfate as the final electron acceptor (see Eq.
629 (2)).

630 At Central Seep, the increase in TA due to the AOM reaction plausibly explains the
631 precipitation of isotopically depleted authigenic carbonates. Particularly, ANME-2
632 biomarkers have been reported in association with abundant fibrous, often botryoidal
633 aragonite cements (Leefmann et al., 2008), which is in line with the observations made at
634 the Central Seep (see Sect. 3.3). Moreover, the high abundance of ANME-2 indicates that
635 seep carbonate formation took place under high sulfate concentrations, strong advective
636 methane flow, but no elevated water temperatures (c.f. Nauhaus et al., 2005; Peckmann et

637 al., 2009; Timmers et al., 2015). Minor amounts of typical marine sterols also show that the
638 seep carbonates also captured detritus from the surrounding sediment and water column
639 during their ongoing cementation.

640 The bulk carbonate carbon isotope signature ($\delta^{13}\text{C}_{\text{V-PDB}} = -46.6\text{‰}$) overlaps with the shallow
641 heavy $\delta^{13}\text{C}_{\text{CH}_4}$ values (-27.5 and -48.6 ‰) in the pore fluids at Central Seep and confirms a
642 dominant AOM signature with a minor planktonic and potentially $\delta^{13}\text{C}$ diluting background
643 signal. The oxygen isotopes point to a low formation temperature of about 3°C, consistent
644 with a precipitation in bottom waters (2.8 to 3.0°C (Fig. 6, 9; Table S4). The $^{87}\text{Sr}/^{86}\text{Sr}$ analyses
645 support this assumption by values within uncertainty identical to modern seawater. U-Th
646 carbonate dating provide ages younger than 240 yrs BP. Summarizing, authigenic carbonates
647 originate from shallow methane and were sub-recently formed in ambient seawater.

648

649 4.3.3 Timing of off-axis hydrothermal activity

650

651 The seismic data taken across the seep locations indicate that the disrupted sediment layers
652 are not reaching to the sediment surface (Fig. 2a, c). This implies that fluid mobilization
653 ceased at some time before the uppermost sediment layers were deposited. The doming
654 above the Central Seep provides some clues on the timing of fluid migration (Fig. 2c).
655 Assuming that the doming is the result of buoyancy-related uplift (Koch et al., 2015) it
656 represents the time when intrusion-related gas reached the seafloor. Assuming further a
657 sedimentation rate of 1.7 m per 1000 years (Central Seep; Table 1) and maxima and minima
658 deposition depths of 48 and 12 m below seafloor, respectively (see Fig. 2c) this would imply
659 that most of the gas reached the seafloor between 28 and 7 kyrs ago. Even at maxima and
660 minima sedimentation rates of 3.5 m (North Seep) and 0.5 m (Ring Seep) per 1000 years, gas
661 flow would have ceased between 14 and 3 kyrs ago at the earliest and between 96 and 24
662 kyrs ago at the latest. Accordingly, this finding further supports the results of the pore fluid
663 and gas geochemistry which show no sign of active fluid flow from depth at the cold seep
664 sites in the northern Guaymas Basin.

665 We agree with Lizarralde et al. (2010) that hydrothermal activity in the Guaymas Basin is an
666 important driver for CH_4 (and CO_2) emissions into bottom waters. However, our data set
667 shows that there is no deep fluid advection at the investigated sites. Our interpretation is
668 that hydrothermal activity at these off-axis locations has ceased and previously formed

669 pathways seem to mediate the advection of biogenic gas at present. It is not unlikely that
670 seep-induced, hydrothermal activity is still ongoing in other places than those investigated in
671 this study, but in order to provide more accurate predictions for (thermogenic) carbon fluxes
672 and the potential impact on climate, sill emplacement mechanisms need to be better
673 constrained. Apart from their spatial distribution, the most important and currently
674 unknown factors are the determination of the time of their emplacement and the longevity
675 of the sill-systems that require further investigation.

676

677 **5 Conclusions**

678

679 Magmatic sill intrusions into organic-rich sediments can potentially release large amounts of
680 carbon into the water column and atmosphere and are therefore considered as potential
681 trigger mechanisms for rapid climate change, e.g. during the PETM. Sill-induced
682 hydrothermalism has been reported along the ridge axis in the Guaymas Basin (von Damm et
683 al., 1985; Berndt et al. 2016) and the widespread occurrence of sills and fluid escape features
684 within the basin has been used to estimate the related carbon release (Lizarralde et al.
685 2010). Our investigations of off-axis methane seeps in the Guaymas Basin demonstrate that
686 there are no indications for hydrothermal activity away from ridge axis at present. These
687 conclusions are mainly based on the lack of geochemical signals from high temperature
688 alteration processes and CH₄ predominantly originating from microbial degradation. We
689 suggest that hydrothermal circulation has, based on seismic records and dating of authigenic
690 carbonates, largely ceased at the investigated sites roughly some thousand years ago. This
691 finding underlines that the vigorous venting, as presently observed at the ridge axis, is a very
692 effective way to release sedimentary carbon into the water column, but must be considered
693 as a very short-lived process in a geological sense. Hence, a more comprehensive
694 understanding of these hydrothermal systems with respect to their climate relevance
695 requires a better knowledge on the control mechanisms and their longevity.

696

697 **Acknowledgments**

698

699 This work was undertaken within the MAKS project funded by the German Ministry of
700 Science and Education (BMBF). We thank the master and crew of the R/V Sonne for their

701 support during the SO241 cruise. Further thanks goes to Regina Surberg, Bettina Domeyer,
702 and Anke Bleyer for analytical support during the cruise and on shore. We greatly appreciate
703 the support from Ana Kolevica, Tyler Goepfert, Sebastian Fessler, Andrea Bodenbinder, Yan
704 Shen, and Jutta Heinze for onshore analyses. Additional support of this work was provided
705 by EU-COST Action ES1301 "FLOWS" (www.flows-cost.eu).

706

707 **References**

708 Aarnes, I., Svensen, H., Connolly, J. A. D. and Podladchikov, Y. Y.: How contact metamorphism can
709 trigger global climate changes: Modeling gas generation around igneous sills in sedimentary basins,
710 *Geochim. Cosmochim. Acta*, 74(24), 7179–7195, doi:10.1016/j.gca.2010.09.011, 2010.

711 Aloisi, G., Drews, M., Wallmann, K. and Bohrmann, G.: Fluid expulsion from the Dvurechenskii mud
712 volcano (Black Sea). Part I. Fluid sources and relevance to Li, B, Sr, I and dissolved inorganic nitrogen
713 cycles, *Earth Planet. Sci. Lett.*, 225(3–4), 347–363, doi:10.1016/j.epsl.2004.07.006, 2004.

714 Bani-Hassan, N.: Numerical modeling of submarine hydrothermal fluid flow, Dr. Diss., 2012.

715 Berndt, C., Hensen, C., Mortera-Gutierrez, C., Sarkar, S., Geilert, S., Schmidt, M., Liebetrau, V., Kipfer,
716 R., Scholz, F., Doll, M., Muff, S., Karstens, J., Planke, S., Petersen, S., Böttner, C., Chi, W.-C., Moser, M.,
717 Behrendt, R., Fiskal, A., Lever, M. A., Su, C.-C., Deng, L., Brennwald, M. S. and Lizarralde, D.: Rifting
718 under steam – how rift magmatism triggers methane venting from sedimentary basins, *Geology*,
719 44(9), 767–770, 2016.

720 Biddle, J. F., Cardman, Z., Mendlovitz, H., Albert, D. B., Lloyd, K. G., Boetius, A. and Teske, A.:
721 Anaerobic oxidation of methane at different temperature regimes in Guaymas Basin hydrothermal
722 sediments, *ISME J.*, 6(5), 1018–1031, doi:10.1038/ismej.2011.164, 2012.

723 Blumenberg, M., Seifert, R., Reitner, J., Pape, T. and Michaelis, W.: Membrane lipid patterns typify
724 distinct anaerobic methanotrophic consortia, *Proc. Natl. Acad. Sci. USA*, 101, 11111–11116, 2004.

725 Calvert, S. E.: Accumulation of Diatomaceous Silica in the Sediments of the Gulf of California, *Geol.*
726 *Soc. Am. Bull.*, 77(June), 569–596, 1966.

727 Campbell, A. C. and Gieskes, J. M.: Water column anomalies associated with hydrothermal activity in
728 the Guaymas Basin, Gulf of California Andrew C. Campbell and Joris M. Gieskes, *Earth Planet. Sci.*
729 *Lett.*, 68, 57–72, 1984.

730 Chan, L. H., Gieskes, J. M., You, C. F. and Edmond, J. M.: Lithium Isotope Geochemistry of Sediments
731 and Hydrothermal Fluids of the Guaymas Basin, Gulf of California, *Geochim. Cosmochim. Acta*,
732 58(20), 4443–4454, 1994.

733 Curray, J. R. and Moore, D. G. et al.: Initial Reports of the Deep Sea Drilling Project. vol. 64., U.S.
734 Govt. Printing Office, Washington., 1982.

735 Von Damm, K. L., Edmond, J. M., Measures, C. I. and Grant, B.: Chemistry of submarine hydrothermal
736 solutions at Guaymas Basin, Gulf of California, *Geochim. Cosmochim. Acta*, 49(11), 2221–2237, 1985.

737 Von Damm, K.: Seafloor Hydrothermal Activity: Black Smoker Chemistry And Chimneys, *Annu. Rev.*
738 *Earth Planet. Sci.*, 18(1), 173–204, doi:10.1146/annurev.earth.18.1.173, 1990.

739 DeMaster, D.: The supply and accumulation of silica in the marine environment, *Geochim.*

- 740 *Cosmochimica Acta*, 5, 1715–1732, 1981.
- 741 Dickens, G. R.: Rethinking the global carbon cycle with a large, dynamic and microbially mediated gas
742 hydrate capacitor, *Earth Planet. Sci. Lett.*, 213(3–4), 169–183, doi:10.1016/S0012-821X(03)00325-X,
743 2003.
- 744 Dowell, F., Cardman, Z., Dasarathy, S., Kellermann, M. Y., Lipp, J. S., Ruff, S. E., Biddle, J. F., McKay, L.
745 J., MacGregor, B. J., Lloyd, K. G., Albert, D. B., Mendlovitz, H., Hinrichs, K. U. and Teske, A.: Microbial
746 communities in methane- and short chain alkane-rich hydrothermal sediments of Guaymas Basin,
747 *Front. Microbiol.*, 7(JAN), doi:10.3389/fmicb.2016.00017, 2016.
- 748 Einsele, G., Gieskes, J. M., Curray, J., Moore, D. M., Aguayo, E., Aubry, M.-P., Fornari, D., Guerrero, J.,
749 Kastner, M., Kelts, K., Lyle, M., Matoba, Y., Molina-Cruz, A., Niemitz, J., Rueda, J., Saunders, A.,
750 Schrader, H., Simoneit, B. and Vacquier, V.: Intrusion of basaltic sills into highly porous sediments,
751 and resulting hydrothermal activity, *Nature*, 283, 441–445, doi:10.1017/CBO9781107415324.004,
752 1980.
- 753 Fisher, A. T. and Becker, K.: Heat flow, hydrothermal circulation and basalt intrusions in the Guaymas
754 Basin, Gulf of California, *Earth Planet. Sci. Lett.*, 103(1–4), 84–99, doi:10.1016/0012-821X(91)90152-
755 8, 1991.
- 756 Gamo, T., Sakai, H., Kim, E.-S., Shitashima, K. and Ishibashi, J. -i.: High-alkalinity due to sulfate
757 reduction in the CLAM hydrothermal field, Okinawa Trough, *Earth planet. Sci. Lett.*, 107, 328–338,
758 1991.
- 759 Gieskes, J. M., Kastner, M., Einsele, G., Kelts, K. and Niemitz, J.: Hydrothermal Activity in the Guaymas
760 Basin, Gulf of California: A synthesis, in *Initial Reports of the Deep Sea Drilling Project*. vol. 64, Pt.
761 2, edited by D. G. et al. Curray, J.R., Moore, pp. 1159–1167., 1982.
- 762 Gieskes, J. M., Gamo, T. and Brumsack, H.: Chemical methods for interstitial water analysis aboard
763 Joides Resolution, *Ocean Drill. Prog. Tech. Note 15*. Texas A&M Univ. Coll. Stn., 1991.
- 764 Goldsmith, J. R., Graf, D. L. and Heard, H. C.: Lattice constants of the calcium-magnesium carbonates,
765 *Am. Miner.*, 46, 453–457, 1961.
- 766 Grasshoff, K., Erhardt, M. and Kremling, K.: *Methods of Seawater Analysis*, Wiley-VCH, Weinheim.,
767 2002.
- 768 Gutjahr, M., Ridgwell, A., Sexton, P. F., Anagnostou, E., Pearson, P. N., Pälike, H., Norris, R. D.,
769 Thomas, E. and Foster, G. L.: Very large release of mostly volcanic carbon during the Palaeocene–
770 Eocene Thermal Maximum, *Nature*, 548(7669), 573–577, doi:10.1038/nature23646, 2017.
- 771 Hartmann, A. and Villinger, H.: Inversion of marine heat flow measurements by expansion of the
772 temperature decay function, *Geophys. J. Int.*, 148(3), 628–636, doi:10.1046/j.1365-
773 246X.2002.01600.x, 2002.
- 774 Henry, P., Le Pichon, X., Lallement, S., Lance, S., Martin, J. B., Foucher, J. P., Fiala-Médioni, A., Rostek,
775 F., Guilhaumou, N., Pranal, V. and Castrec, M.: Fluid flow in and around a mud volcano seaward of
776 the Barbados accretionary wedge: Results from Manon cruise, *J. Geophys. Res.*, 101(9), 20297–
777 20323, 1996.
- 778 Hensen, C., Nuzzo, M., Hornibrook, E., Pinheiro, L. M., Bock, B., Magalhães, V. H. and Brückmann, W.:
779 Sources of mud volcano fluids in the Gulf of Cadiz-indications for hydrothermal imprint, *Geochim.*
780 *Cosmochim. Acta*, 71(5), 1232–1248, doi:10.1016/j.gca.2006.11.022, 2007.
- 781 Hinrichs, K.-U., Pancost, R. D., Summons, R. E., Sprott, G. D., Sylva, S. P., Sinninghe Damsté, J. S. and

- 782 Hayes, J. M.: Mass spectra of sn -2-hydroxyarchaeol, a polar lipid biomarker for anaerobic
783 methanotrophy, *Geochemistry Geophys. Geosystems*, 1, 11–13, 2000.
- 784 Howarth, R. J. and McArthur, J. M.: Strontium isotope stratigraphy, in *A Geological Time Scale, with*
785 *Look-up Table Version 4*, edited by F. M. Gradstein and J. G. Ogg, pp. 96–105, Cambridge University
786 Press, Cambridge, U.K pp. ., 2004.
- 787 Huh, C.-A., Su, C.-C., Wang, C.-H., Lee, S.-Y. and Lin, I.-T.: Sedimentation in the Southern Okinawa
788 Trough – Rates, turbidites and a sediment budget, *Mar. Geol.*, 231, 129–139, 2006.
- 789 Ivanenkov, V. N. and Lyakhin, Y. I.: Determination of total alkalinity in seawater, in *In Methods of*
790 *Hydrochemical Investigations in the Ocean*, edited by O. K. Bordovsky and V. N. Ivanenkov, p. 110–
791 114 (in Russian), Nauka Publishing House, Moscow., 1978.
- 792 Iyer, K., Schmid, D. W., Planke, S. and Millett, J.: Modelling hydrothermal venting in volcanic
793 sedimentary basins: Impact on hydrocarbon maturation and paleoclimate, *Earth Planet. Sci. Lett.*,
794 467, 30–42, doi:10.1016/j.epsl.2017.03.023, 2017.
- 795 Jahnke, R. A., Emerson, S. R. and Murray, J. W.: A model of oxygen reduction, denitrification, and
796 organic matter mineralization in marine sediments, *Limnol. Oceanogr.*, 27(4), 610–623,
797 doi:10.4319/lo.1982.27.4.0610, 1982.
- 798 Karaca, D., Hensen, C. and Wallmann, K.: Controls on authigenic carbonate precipitation at cold seeps
799 along the convergent margin off Costa Rica, *Geochemistry, Geophys. Geosystems*, 11(8), 1–19,
800 doi:10.1029/2010GC003062, 2010.
- 801 Kastner, M.: Evidence for Two Distinct Hydrothermal Systems in the Guaymas Basin, in *In Initial*
802 *Reports of the Deep Sea Drilling Project. vol. 64, Pt. 2*, edited by D. G. et al. Curray, J.R., Moore, pp.
803 1143–1157, U.S. Govt. Printing Office, Washington., 1982.
- 804 Kastner, M. and Siever, R.: Siliceous Sediments of the Guaymas Basin: The Effect of High Thermal
805 Gradients on Diagenesis, *J. Geol.*, 91(6), 629–641, doi:10.1086/628816, 1983.
- 806 Kinoshita, M. and Yamano, M.: Hydrothermal regime and constraints on reservoir depth of the Jade
807 site in the Mid-Okinawa Trough inferred from heat flow measurements, *J. Geophys. Res.*, 102(B2),
808 3183–3194, 1997.
- 809 Koch, S., Berndt, C., Bialas, J., Haeckel, M., Crutchley, G., Papenberg, C., Klaeschen, D. and Greinert,
810 J.: Gas-controlled seafloor doming, *Geology*, 43(7), 571–574, doi:doi: 10.1130/G36596.1, 2015.
- 811 Lee, S.-Y., Huh, C.-A., Su, C.-C. and You, C.-F.: Sedimentation in the Southern Okinawa Trough:
812 enhanced particle scavenging and teleconnection between the Equatorial Pacific and western Pacific
813 margins, *Deep. Res.*, 51, 1769–1780, 2004.
- 814 Leefmann, T., Bauermeister, J., Kronz, A., Liebetrau, V., Reitner, J. and Thiel, V.: Miniaturized
815 biosignature analysis reveals implications for the formation of cold seep carbonates at Hydrate Ridge
816 (off Oregon, USA), *Biogeosciences*, 5, 731–738, 2008.
- 817 Lizarralde, D., Soule, S. A., Seewald, J. S. and Proskurowski, G.: Carbon release by off-axis magmatism
818 in a young sedimented spreading centre, *Nat. Geosci.*, 4(1), 50–54, doi:10.1038/ngeo1006, 2010.
- 819 Lonsdale, P. and Becker, K.: Hydrothermal plumes, hot springs, and conductive heat flow in the
820 Southern Trough of Guaymas Basin, *Earth Planet. Sci. Lett.*, 73(2–4), 211–225, doi:10.1016/0012-
821 821X(85)90070-6, 1985.
- 822 Lupton, J. E.: Helium-3 in the Guaymas Basin: Evidence for injection of mantle volatiles in the Gulf of

- 823 California, J. Geophys. Res., 84(B13), 7446, doi:10.1029/JB084iB13p07446, 1979.
- 824 McDermott, J. M., Seewald, J. S., German, C. R. and Sylva, S. P.: Pathways for abiotic organic synthesis
825 at submarine hydrothermal fields, PNAS, 112(25), 7668–7672, 2015.
- 826 Milkov, A. V., Claypool, G. E., Lee, Y. J. and Sassen, R.: Gas hydrate systems at Hydrate Ridge offshore
827 Oregon inferred from molecular and isotopic properties of hydrate-bound and void gases, Geochim.
828 Cosmochim. Acta, 69(4), 1007–1026, doi:10.1016/j.gca.2004.08.021, 2005.
- 829 Nauhaus, K., Treude, T., Boetius, A. and Krüger, M.: Environmental regulation of the anaerobic
830 oxidation of methane: A comparison of ANME-I and ANME-II communities, Environ. Microbiol, 7, 98–
831 106, 2005.
- 832 Niemann, H. and Elvert, M.: Diagnostic lipid biomarker and stable isotope signatures of microbial
833 communities mediating the anaerobic oxidation of methane with sulphate, Org. Geochem., 39,
834 1668–1677, 2008.
- 835 Peckmann, J., Birgel, D. and Kiel, S.: Molecular fossils reveal fluid composition and flow intensity at a
836 Cretaceous seep, Geology, 37, 847–850, 2009.
- 837 Pfender, M. and Villinger, H.: Miniaturized data loggers for deep sea sediment temperature gradient
838 measurements, Mar. Geol., 186(3–4), 557–570, doi:10.1016/S0025-3227(02)00213-X, 2002.
- 839 Sahling, H., Rickert, D., Lee, R. W., Linke, P. and Suess, E.: Sahiling -macro-muc, , 231, 121–138, 2002.
- 840 Schmidt, M., Hensen, C., Mörz, T., Müller, C., Grevemeyer, I., Wallmann, K., Mau, S. and Kaul, N.:
841 Methane hydrate accumulation in “Mound 11” mud volcano, Costa Rica forearc, Mar. Geol., 216(1–
842 2), 83–100, doi:10.1016/j.margeo.2005.01.001, 2005.
- 843 Schmidt, M., Linke, P., Sommer, S., Esser, D. and Cherednichenko, S.: Natural CO₂ Seeps Offshore
844 Panarea : A Test Site for Subsea CO₂ Leak Detection Limit, Mar. Technol. Soc. J., 49(1), 19–30, 2015.
- 845 Scholz, F., Hensen, C., Reitz, A., Romer, R. L., Liebetrau, V., Meixner, A., Weise, S. M. and Haeckel, M.:
846 Isotopic evidence (⁸⁷Sr/⁸⁶Sr, δ^7 Li) for alteration of the oceanic crust at deep-rooted mud volcanoes
847 in the Gulf of Cadiz, NE Atlantic Ocean, Geochim. Cosmochim. Acta, 73(18), 5444–5459,
848 doi:10.1016/j.gca.2009.06.004, 2009.
- 849 Scholz, F., Hensen, C., De Lange, G. J., Haeckel, M., Liebetrau, V., Meixner, A., Reitz, A. and Romer, R.
850 L.: Lithium isotope geochemistry of marine pore waters - Insights from cold seep fluids, Geochim.
851 Cosmochim. Acta, 74(12), 3459–3475, doi:10.1016/j.gca.2010.03.026, 2010.
- 852 Simoneit, B. R. T., Leif, R. N., Sturz, A. A., Sturdivant, A. E. and Gieskes, J. M.: Geochemistry of shallow
853 sediments in Guaymas Basin, gulf of California: hydrothermal gas and oil migration and effects of
854 mineralogy, Org. Geochem., 18(6), 765–784, doi:10.1016/0146-6380(92)90046-Z, 1992.
- 855 Sommer, S., Linke, P., Pfannkuche, O., Schleicher, T., Deimling, J. S. V, Reitz, A., Haeckel, M., Flögel, S.
856 and Hensen, C.: Seabed methane emissions and the habitat of frenulate tubeworms on the Captain
857 Arutyunov mud volcano (Gulf of Cadiz), Mar. Ecol. Prog. Ser., 382, 69–86, doi:10.3354/meps07956,
858 2009.
- 859 Śródoń, J.: Nature of Mixed-Layer Clays and Mechanisms of Their Formation and Alteration, Annu.
860 Rev. Earth Planet. Sci., 27(1), 19–53, doi:10.1146/annurev.earth.27.1.19, 1999.
- 861 Svensen, H., Planke, S., Malthe-Sorensen, A., Jamtveit, B., Myklebust, R., Eidem, T. R. and Rey, S. S.:
862 Release of methane from a volcanic basin as a mechanism for initial Eocene global warming, Nature,
863 429(June), 3–6, doi:10.1038/nature02575.1., 2004.

- 864 Teske, A., Callaghan, A. V. and LaRowe, D. E.: Biosphere frontiers of subsurface life in the sedimented
865 hydrothermal system of Guaymas Basin, *Front. Microbiol.*, 5(JULY), 1–11,
866 doi:10.3389/fmicb.2014.00362, 2014.
- 867 Teske, A., De Beer, D., McKay, L. J., Tivey, M. K., Biddle, J. F., Hoer, D., Lloyd, K. G., Lever, M. A., Røy,
868 H., Albert, D. B., Mendlovitz, H. P. and MacGregor, B. J.: The Guaymas Basin hiking guide to
869 hydrothermal mounds, chimneys, and microbial mats: Complex seafloor expressions of subsurface
870 hydrothermal circulation, *Front. Microbiol.*, 7(FEB), 1–23, doi:10.3389/fmicb.2016.00075, 2016.
- 871 Timmers, P. H., Widjaja-Greefkes, H.A. Ramiro-Garcia, J., Plugge, C. M. and Stams, A. J.: Growth and
872 activity of ANME clades with different sulfate and sulfide concentrations in the presence of methane,
873 *Front. Microbiol.*, 6, 988, 2015.
- 874 Wallmann, K., Drews, M., Aloisi, G. and Bohrmann, G.: Methane discharge into the Black Sea and the
875 global ocean via fluid flow through submarine mud volcanoes, *Earth Planet. Sci. Lett.*, 248(1–2), 544–
876 559, doi:10.1016/j.epsl.2006.06.026, 2006.
- 877 Wegener, G., Krukenberg, V., Ruff, S. E., Kellermann, M. Y. and Knittel, K.: Metabolic capabilities of
878 microorganisms involved in and associated with the anaerobic oxidation of methane, *Front.*
879 *Microbiol.*, 7, 46, 2016.
- 880 Welhan, J. A.: Origins of methane in hydrothermal systems, *Chem. Geol.*, 71(1–3), 183–198,
881 doi:10.1016/0009-2541(88)90114-3, 1988.
- 882 Whiticar, M. J.: Carbon and hydrogen isotope systematics of bacterial formation and oxidation of
883 methane, , 161, 291–314, 1999.
- 884 Zachos, J. C., Wara, M. W., Bohaty, S., Delaney, M. L., Petrizzo, M. R., Brill, A., Bralower, T. J. and
885 Premoli-Silva, I.: A transient rise in tropical sea surface temperature during the Paleocene-Eocene
886 thermal maximum., *Science*, 302(5650), 1551–1554, doi:10.1126/science.1090110, 2003.

887

888 Tables

889

890 Table 1: Station list and site names of GCs and MUCs taken in the Guaymas Basin with
891 according water depth. Heat flow and temperature gradient data measured either attached
892 to GCs or to a sediment probe.

Site	Site name	Latitude (N)	Longitude (W)	Water depth (m)	Temp. gradient (K m ⁻¹)	Heat flow (mW m ⁻²)	SR (m kyr ⁻¹)	MAR (g cm ⁻² yr ⁻¹)
GCs								
St.07-GC01	North Seep	27° 33.301'	111° 32.882'	1845	0.14	28	n.d.	n.d.
St.10-GC04	Reference Site	27° 26.531'	111° 29.928'	1846	0.22	140	n.d.	n.d.
St.09-GC03	Central Seep	27° 28.138'	111° 28.420'	1837	n.d.	n.d.	n.d.	n.d.
St.09-GC13	Central Seep	27° 28.193'	111° 28.365'	1838	0.16	113	n.d.	n.d.
St.72-GC15	Central Seep	27° 28.178'	111° 28.396'	1837	n.d.	n.d.	n.d.	n.d.

St.51-GC09	Smoker Site	27° 24.472'	111° 23.377'	1840	11	8069	n.d.	n.d.
St.58-GC10	Smoker Site	27° 24.478'	111° 23.377'	1845	10	6509	n.d.	n.d.
St.47-GC07	Slope Site	27° 24.412'	111° 13.649'	671	n.d.	n.d.	n.d.	n.d.
MUCs								
St.33-MUC11	North Seep	27° 33.301'	111° 32.883'	1855	n.d.	n.d.	1.7*	0.05*
							3.5 [#]	0.15 [#]
St.23-MUC05	Ring Seep	27° 30.282'	111° 40.770'	1726	n.d.	n.d.	0.5	0.01
St.15-MUC02	Reference Site	27° 26.925'	111° 29.926'	1845	n.d.	n.d.	2.3	0.04
St.22-MUC04	Central Seep	27° 28.165'	111° 28.347'	1839	n.d.	n.d.	1.7	0.04
St.65-MUC15	Smoker Site	27° 24.342'	111° 22.970'	1846	n.d.	n.d.	1.8	0.05
St.66-MUC16	Smoker Site	27° 24.577'	111° 23.265'	1842	n.d.	n.d.	2.1'	0.08'
							0.4 ⁺	0.02 ⁺
HF lance								
St.60a - HF008_P03	Smoker Site	27° 24.273'	111° 23.396'	1840	4.6	3206	n.a.	n.a.
St.60a - HF008_P01		27° 24.623'	111° 23.626'	1834	0.86	599	n.a.	n.a.
St.60a - HF008_P02		27° 24.554'	111° 23.512'	1840	2.8	1953	n.a.	n.a.
St.60a - HF008_P04		27° 24.408'	111° 23.288'	1849	2039	1427	n.a.	n.a.
St.60a - HF008_P05		27° 24.341'	111° 23.177'	1852	1014	710	n.a.	n.a.
St.60a - HF008_P06		27° 24.265'	111° 23.082'	1844	0.74	516	n.a.	n.a.
St.60b - HF008_P07		27° 24.193'	111° 23.956'	1834	0.8	579	n.a.	n.a.
St.60b - HF009_P04		27° 24.543'	111° 23.351'	1837	15	10835	n.a.	n.a.
St.60b - HF009_P01		27° 24.605'	111° 23.317'	1837	0.39	274	n.a.	n.a.
St.60b - HF009_P02		27° 24.552'	111° 23.347'	1834	3451	2415	n.a.	n.a.
St.70 - HF011_P01	Graben Site	27° 25.802'	111° 25.486'	1870	0.38	262	n.a.	n.a.
St.70 - HF011_P02		27° 25.460'	111° 24.946'	2019	0.48	338	n.a.	n.a.
St.70 - HF011_P03		27° 25.955'	111° 24.493'	2046	0.43	302	n.a.	n.a.

St.70 - HF011_P04		27° 25.837'	111° 24.951'	2025	0.46	320	n.a.	n.a.
Authigenic carbonate								
St.56-VgHG-4	Central Seep	27°28.181'	111°28.379'	1843	n.a.	n.a.	n.a.	n.a.

Abbreviations: SR, Sedimentation Rate; MAR, Mass Accumulation Rate; n.d., not determined; n.a., not applicable

*#Sedimentation and mass accumulation rates at Station 33 of the 0-13 cm, 13-18 cm layers, respectively

+Sedimentation and mass accumulation rates at Station 65 of the 0 - 7 cm, 7 - 17 cm layers, respectively

893

894

895 **Figures**

896

897 Figure 1: Sample locations in the Guaymas Basin, Gulf of California studied during RV SONNE
 898 expedition SO241. (a) Overview of stations (Seep Sites, Smoker Site, and Slope Site). Black
 899 square indicates enlargement area in (b). Site DSDP 477 in the southern trough is shown for
 900 comparison. (b) Enlargement of the sampling locations. Red circles refer to GC employments
 901 and yellow triangles to MUCs. Brown square at Graben Site refers to water column sampling
 902 and temperature measurements. Black lines refer to seismic profiles, displayed in Fig. 2. (c)
 903 Enlargement of Smoker Site sampling locations. Note the different scale compared to (a) and
 904 (b). Black arrow refers to the location of the hydrothermal mound described in Berndt et al.
 905 (2016).

906

907 Figure 2: Seismic profiles of North Seep (a), Smoker Site (b) as well as of Central Seep and
 908 Reference Site (c). Seismic section showing doming above the Central Seep. There are
 909 different phases of onlap starting about 60 ms (maximum deposition) until about 15 ms
 910 (minimum deposition) or 48 and 12 mbsf respectively assuming a sediment interval velocity
 911 of 1600 m s^{-1} .

912

913 Figure 3: (a) Heat flow in the vicinity of the northern trough. Note the different heat flow
 914 scale in the enlarged area of the Smoker Site (b).

915

916 Figure 4: Pore water profiles of GCs (a) and MUCs (b). For Central Seep, GC13 is shown
 917 exemplary here, geochemical data of the remaining cores (GC03, 15) can be found in Table

918 S1. Endmember composition of hydrothermal solutions from Von Damm et al. (1985) and
919 hydrothermal plume geochemical composition from Berndt et al. (2016) are shown in (a) for
920 comparison.

921
922 Figure 5. Sr concentrations and $^{87}\text{Sr}/^{86}\text{Sr}$ ratios for GCs (a) and MUCs (b). For comparison,
923 data from the hydrothermal plume (Berndt et al., 2016), the hydrothermal endmember (Von
924 Damm et al., 1985), and modern seawater (Howarth and McArthur, 2004) are shown. Note
925 the different x-axis scales for MUC Sr concentration and $^{87}\text{Sr}/^{86}\text{Sr}$ ratios.

926
927 Figure 6: Water column temperature, salinity, turbidity, and methane concentrations. Note
928 that the upper ~300 m below sea level (bsl) in the turbidity data are not shown for scale
929 matters. VCDT09 and temperature data from VCDT10 are from Berndt et al. (2016), all other
930 parameters were acquired in this study.

931
932 Fig. 7: NH_4 (μM) versus Li concentrations (μM) of Guaymas Basin cold seeps (North, Central)
933 and the Smoker Site. Deep fluids from Smoker Site (GC09) mix with hydrothermal fluids with
934 a share of ~3%. The mixing line has been calculated following: $x_{mix} = x_{phase1} * f_1 +$
935 $x_{phase2} * f_2$ (1), with $f_1 + f_2 = 1$. Endmember 1 is the Guaymas Vent South (Von Damm, 1985,
936 1990) and endmember 2 is Guaymas North Seep. For comparison, Guaymas hydrothermal
937 endmember fluid composition (Von Damm, 1985, 1990), hydrothermal plume fluid
938 composition (Berndt et al., 2016), Guaymas slope sediments (GC07), and deep-sourced cold
939 seeps (Aloisi et al., 2004; Hensen et al., 2007) are shown.

940
941 Figure 8: Hydrocarbon, $\delta^{13}\text{C}_{\text{CH}_4}$ and δD isotope data for Guaymas Basin seep sites, Smoker
942 and Slope Site. Hydrothermal plume data are shown for comparison. Note that hydrocarbon
943 and $\delta^{13}\text{C}_{\text{CH}_4}$ data are from Berndt et al. (2016). (a) $\text{CH}_4/(\text{C}_2\text{H}_6+\text{C}_3\text{H}_8)$ ratios versus $\delta^{13}\text{C}_{\text{CH}_4}$ data
944 are shown after a modified Bernard diagram (Schmidt et al., 2005). Pale symbols indicate
945 samples above the AOM zone. Rayleigh fractionation lines show the effect of (microbial)
946 methane oxidation, labels indicate the residual methane in %. (b) Carbon ($\delta^{13}\text{C}_{\text{CH}_4}$) and
947 hydrogen ($\delta\text{D}_{\text{CH}_4}$) isotope data after Whiticar (1999) and (Welhan, 1988). Pale symbols
948 (Central Seep (MUC04)) indicate samples above AOM zone.

949

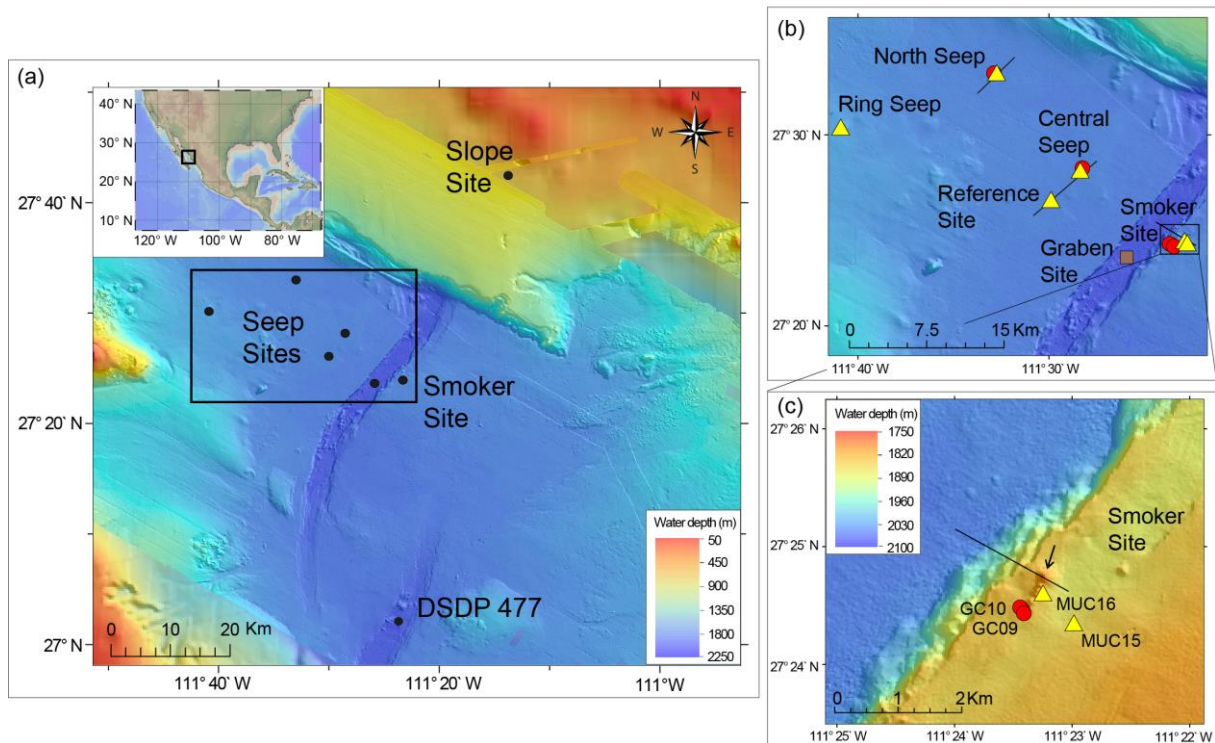
950 Figure 9. Water column CH₄ (a) and temperature (b) at cold seeps as well as Smoker and
951 Graben Site relative to the rift axis.

952

953

954

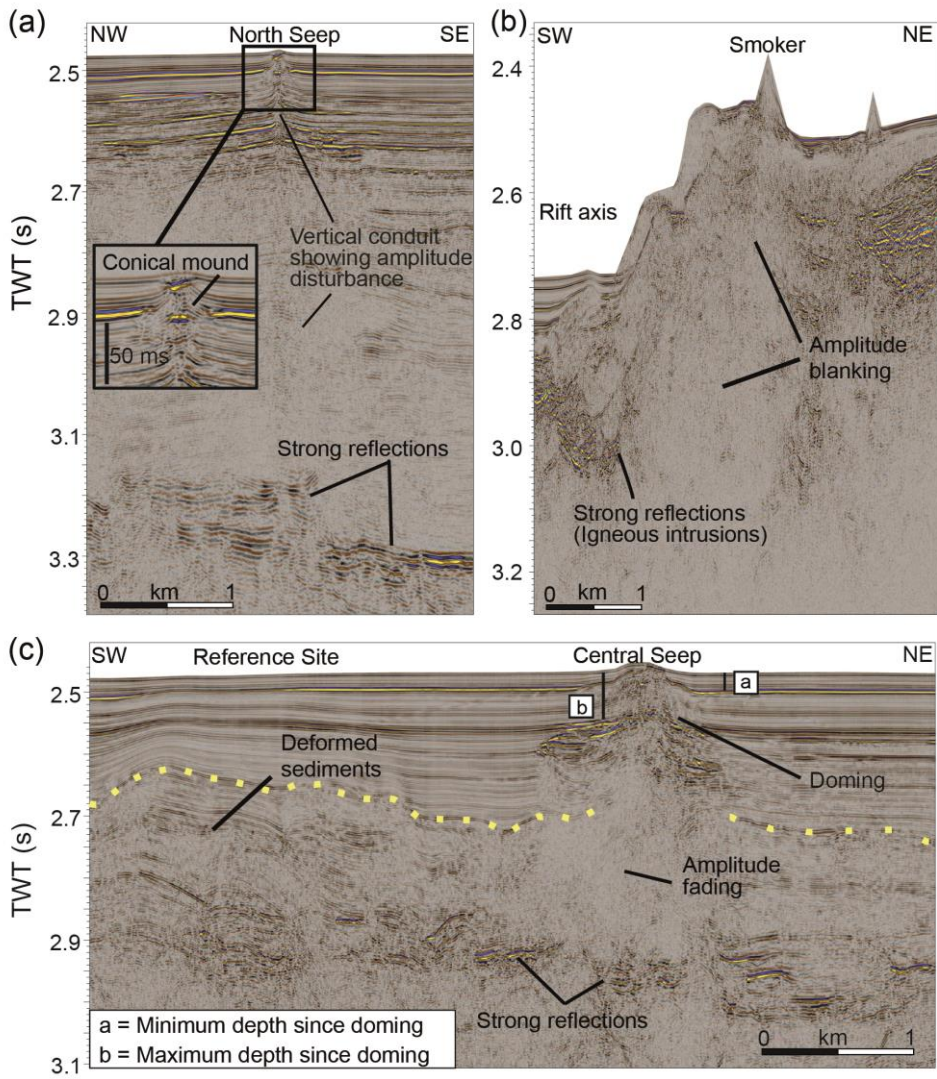
fig01



955

956

fig02



957

fig03

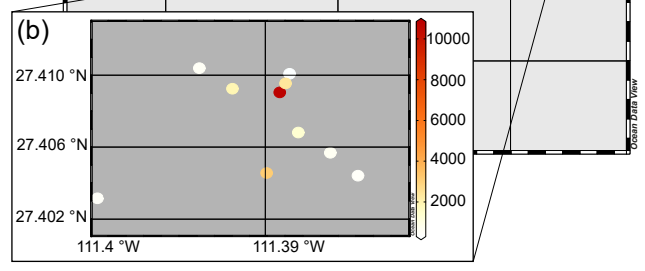
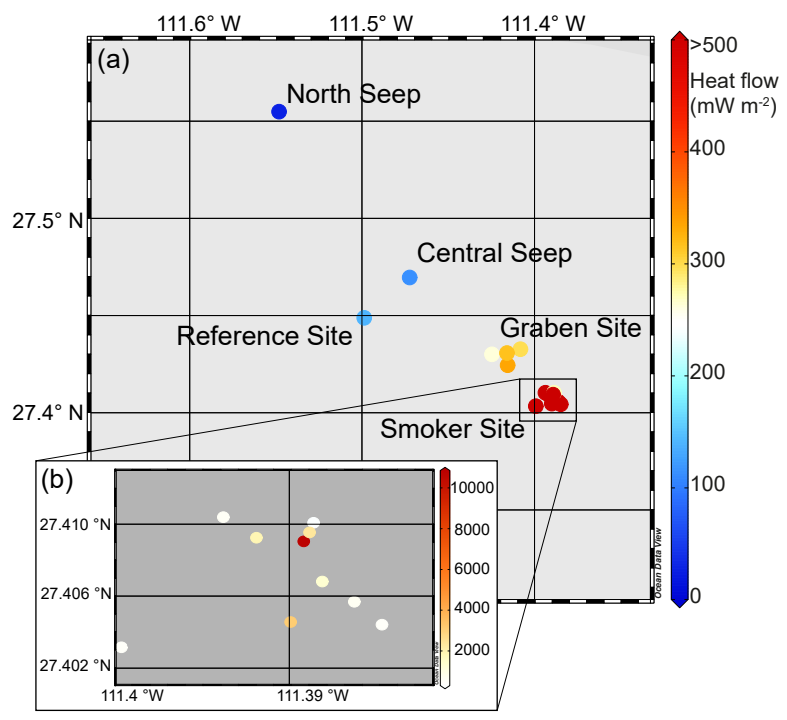


fig04

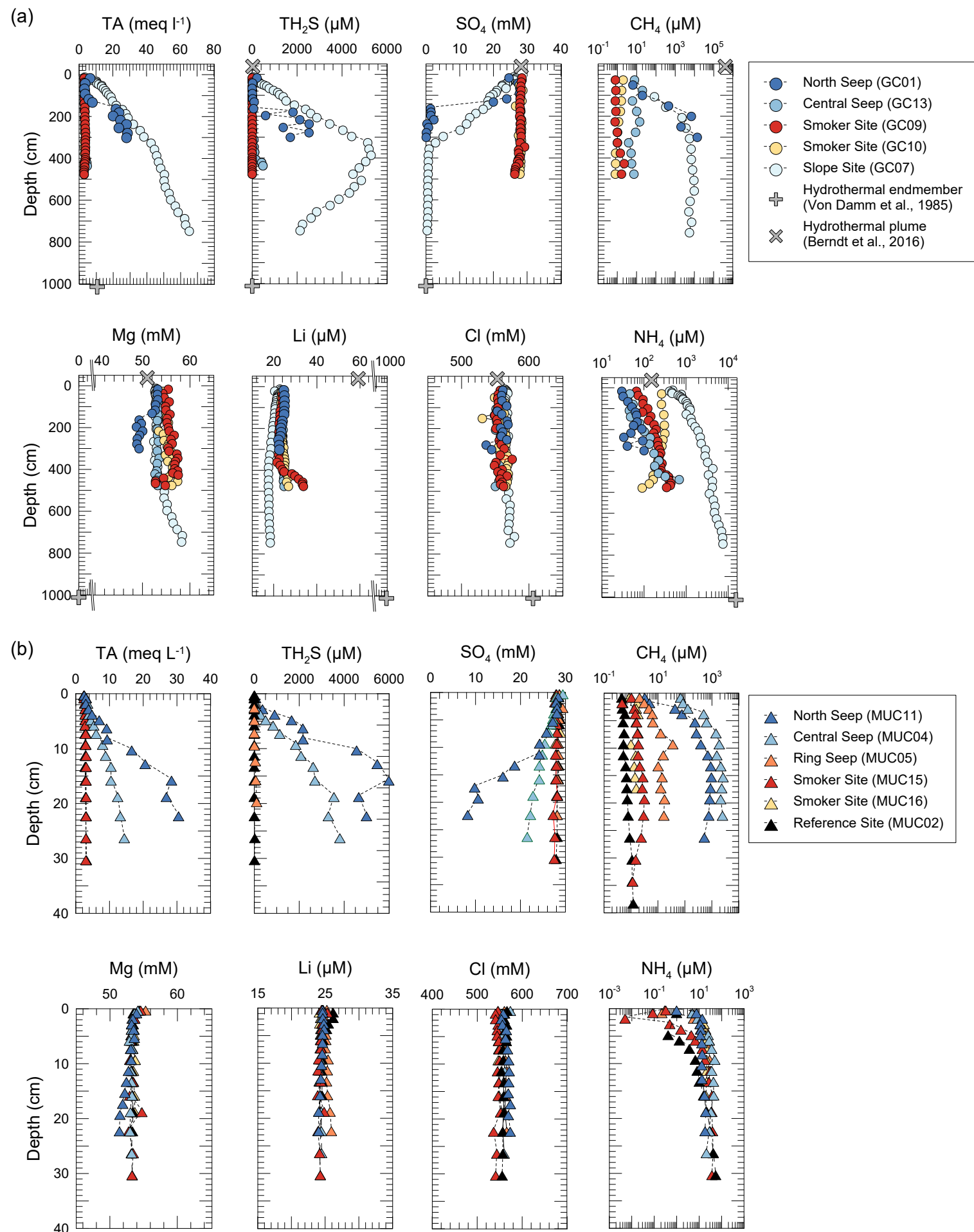


fig05

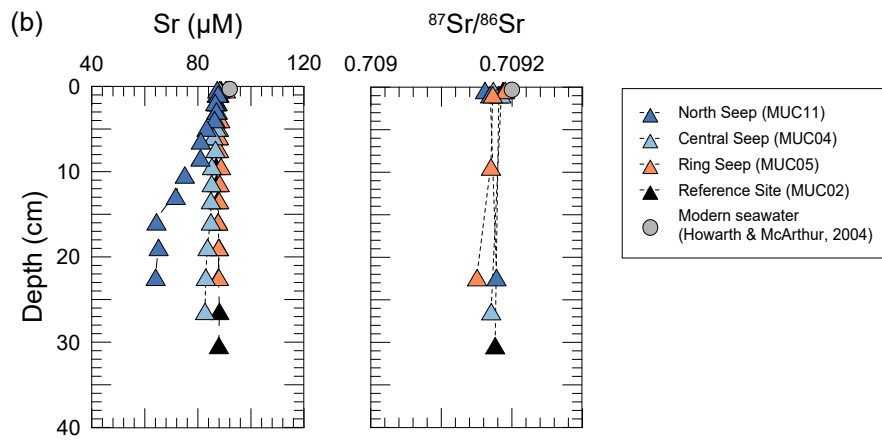
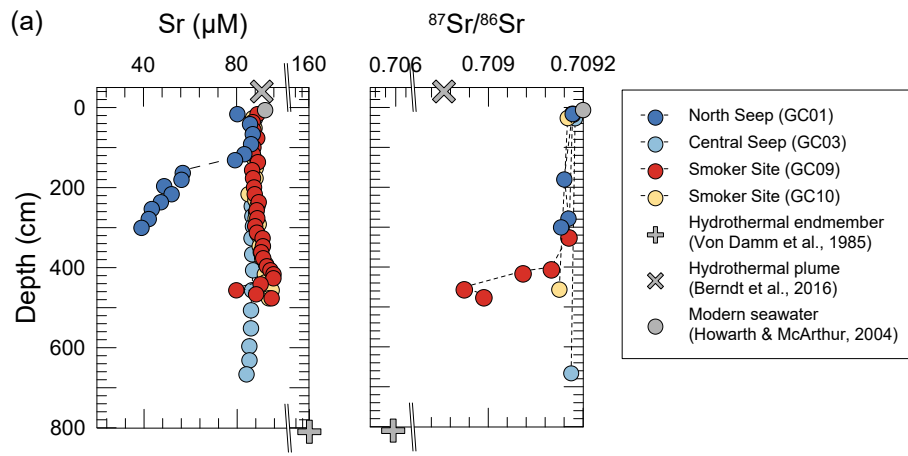


fig06

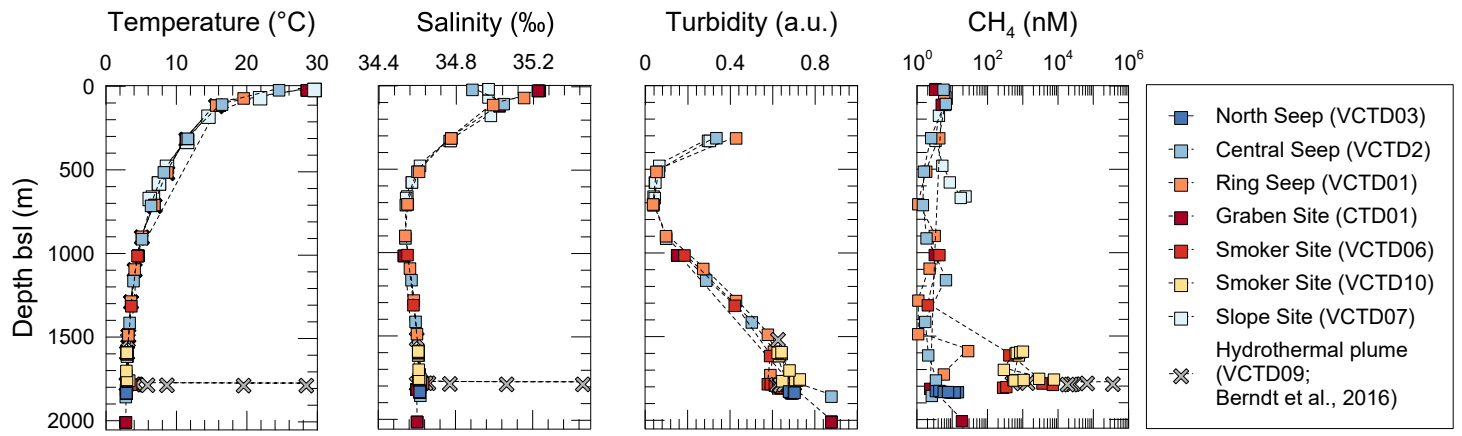


fig07

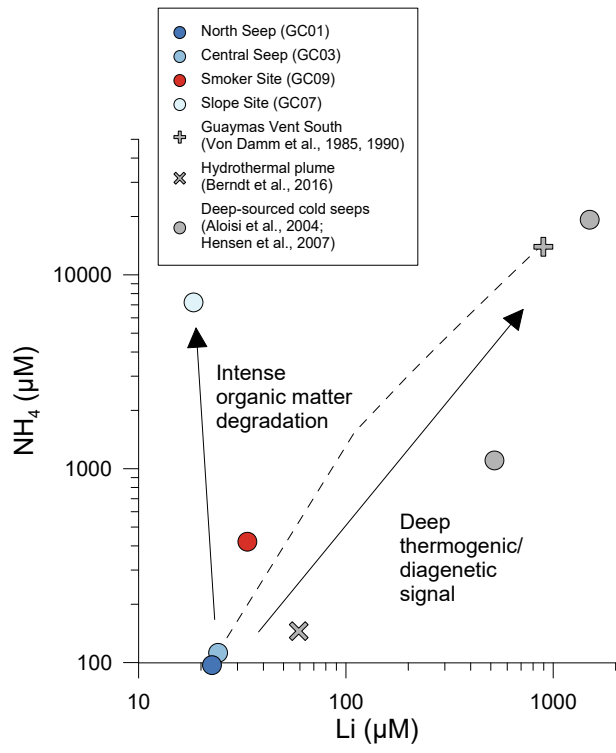
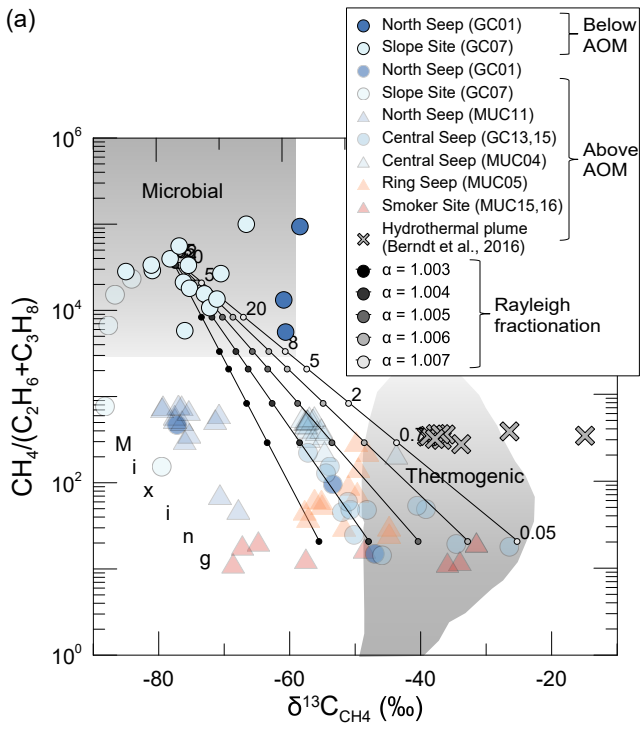


fig08

(a)



(b)

